nature communications

Article

https://doi.org/10.1038/s41467-025-64980-0

Capturing disease severity in LIS1-lissencephaly reveals proteostasis dysregulation in patient-derived forebrain organoids

Received: 25 March 2024

Accepted: 2 October 2025

Lea Zillich[1,2,3,4,15], **Matteo Gasparotto**[1,2,3,15], **Andrea Carlo Rossetti**[1,2,3,15], **Olivia Fechtner**[1,2,3,5,15], **Camille Maillard**[6], **Anne Hoffrichter**[1,2,3], **Eric Zillich**[4], **Ammar Jabali**[1,2,3], **Fabio Marsoner**[1,2,3], **Annasara Artioli**[1,2,3], **Ruven Wilkens**[1,2,3], **Christina B. Schroeter**[7], **Andreas Hentschel**[8], **Stephanie H. Witt**[4], **Nico Melzer**[7], **Sven G. Meuth**[7], **Tobias Ruck**[8,9], **Philipp Koch**[1,2,3], **Andreas Roos**[7,10,11], **Nadia Bahi-Buisson**[6], **Fiona Francis**[12,13,14] & **Julia Ladewig**[1,2,3] ✉

LIS1-lissencephaly is a neurodevelopmental disorder marked by reduced cortical folding and severe neurological impairment. Although all cases result from heterozygous mutations in the *LIS1* gene, patients present a broad spectrum of severity. Here, we use patient-derived forebrain organoids representing mild, moderate, and severe LIS1-lissencephaly to uncover mechanisms underlying this variability. We show that LIS1 protein levels vary across patient lines and partly correlate with clinical severity, indicating mutation-specific effects on protein function. Integrated morphological, transcriptomic, and proteomic analyses reveal progressive changes in neural progenitor homeostasis and neurogenesis that scale with severity. Mechanistically, microtubule destabilization disrupts cell–cell junctions and impairs WNT signaling, and defects in protein homeostasis, causing stress from misfolded proteins, emerge as key severity-linked pathways. Pharmacological inhibition of mTORC1 partially rescues these defects. Our findings demonstrate that patient-derived organoids can model disease severity, enabling mechanistic dissection and guiding targeted strategies in neurodevelopmental disorders.

The human neocortex, critical for higher cognitive functions such as language, sociability, and sensorimotor control, is an extensively folded and highly organized structure[1]. Malformations of cortical development (MCD) disrupt these processes, leading to a spectrum of neurodevelopmental disorders (NDDs), including lissencephaly, which accounts for up to 40% of childhood treatment-refractory epilepsies[2].

LIS1-Lissencephaly (smooth brain) is a severe NDD caused by heterozygous *LIS1* mutations (MIM: 607432), resulting in a spectrum of cortical malformations, from mild pachygyria (broad gyri) to severe agyria (no gyri), accompanied by intellectual disability, epilepsy, and high mortality[3]. While the degree of cortical malformation correlates with clinical severity, the link between specific *LIS1* mutation types or

---

A full list of affiliations appears at the end of the paper. ✉e-mail: Julia.Ladewig@zi-mannheim.de

locations and phenotypic manifestation remains complex and only partially characterized[4].

The LIS1 protein functions as a homodimer and is a key regulator of dynein-dynactin assembly and microtubule motor function[5,6] By enhancing dynein motor processivity, LIS1 supports retrograde transport critical for diverse neurodevelopmental processes, including neuronal migration, axon growth, nuclear migration, centrosome positioning, chromosomal segregation, and mitotic spindle orientation (reviewed in refs. 7,8). LIS1 also influences signaling pathways, including FGF, Cdc42 and WNT[9–11]. Through these functions, LIS1 plays a central role in cortical layer formation and neural progenitor behavior and fate decisions.

Rodent models and clinical studies have implicated both LIS1 protein dosage[12,13] and mutation-specific dysfunction[4] as critical determinants of neurodevelopmental outcome and phenotypic severity. However, whether distinct LIS1 mutations lead to graded reductions in LIS1 protein dosage or function, and how this contributes to the spectrum of cellular and molecular phenotypes, remains unclear. Given the rare accessibility of human postmortem brain tissue from LIS1-lissencephaly patients, direct analysis of human pathology remains scarce, and traditional models fail to fully capture human-specific features, especially gyrification.

Human-based systems are critically needed to address how diverse *LIS1* mutations give rise to variable clinical severity. iPSC-derived cerebral organoids represent a powerful platform for studying human neurodevelopment and MCD[14,15]. These systems recapitulate key features of the fetal cortex, including ventricular zone (VZ), subventricular zone (SVZ) and neuronal layer (NL) formation, and reproduce transcriptomic signatures of the developing human brain across diverse genetic backgrounds[16]. Cerebral organoids have been effectively used to investigate both genetically defined and idiopathic NDDs through isogenic and stratified designs, multi-omics integration, and functional rescue approaches[17], making them uniquely suited for dissecting mechanisms across the LIS1-lissencephaly severity spectrum. Using this platform, LIS1 has previously been linked to basal radial glial (bRG) cell behavior[18,19], a progenitor population enriched in primates and implicated in human cortical expansion[1].

In this study, we focus on earlier stages of cortical development, leveraging patient-derived forebrain (FB) organoids to model LIS1-lissencephaly across a severity gradient. Specifically, we target neuroepithelial (NE) and RG cells, which form the developmental foundation for human cortical growth and stratification[20]. Building on our prior work in Miller–Dieker syndrome (MDS, a severe contiguous gene deletion syndrome involving *LIS*1[9]), where we linked LIS1 dosage to VZ integrity, N-cadherin-mediated β-catenin/WNT signaling, and neurogenesis, we now extend this framework to diverse, genetically distinct *LIS1* mutations. Using this severity-stratification approach, we identified both shared and progressive alterations in cytoarchitecture, progenitor homeostasis, and molecular pathways across mild, moderate, and severe LIS1-lissencephaly. Our findings support a multi-layered model in which LIS1 protein reduction or dysfunction leads to microtubule destabilization, disrupted adherens junctions, impaired WNT signaling, and premature neurogenesis. Importantly, we also identify progressive proteostasis dysregulation, manifesting in ER stress resulting in the activation of unfolded protein response (UPR), as a severity-linked mechanism that extends into late-stage neurons in severe LIS1 organoids. This expands LIS1´s functional role beyond cytoskeletal regulation, including cellular stress and protein homeostasis. Targeted pharmacological interventions validated key disrupted pathways: EpothiloneD (EpoD, microtubule stabilization[21]) rescued structural defects, CHIR99021 (WNT activation[22]) improved division angle abnormalities, and Everolimus (mTORC1 inhibition[23]), identified via in silico drug repurposing, mitigated proteostasis stress and partially restored the neurogenic balance in moderate and severe LIS1-lissencephaly cases.

Together, our findings reveal previously unrecognized molecular mechanisms relevant to pathogenesis and demonstrate that FB organoid-based modeling offers a powerful platform for capturing patient-specific severity gradients and dissecting mechanism–phenotype relationships in NDDs.

Results

Modeling the LIS1-lissencephaly severity spectrum in forebrain organoids reveals progressive structural disruption and premature neurogenesis

To model the spectrum of LIS1-lissencephaly, we selected seven LIS1-patients from a cohort of 63 cases, spanning the full range of gyrification abnormalities[24] (Dobyns grade 5 (mild) to 1 (severe) (Fig. 1A), for more details on MRI data, see Philbert et al.[25]). Each patient carries a molecularly characterized heterozygous pathogenic *LIS1* variant (Supplementary Fig. S1A). Patient selection was based on clinical severity, neuroradiological data[25], and known genotype–phenotype correlations (for details, see the “Methods” section). Given the genetic heterogeneity among patient lines, we established a biologically diverse control group consisting of eight unrelated, well-characterized iPSC lines (two clones each for five of them) from healthy individuals, primarily reflecting the donor age spectrum[26] (Supplementary Data S1). This pooled control strategy serves as a biologically diverse, robust reference for assessing severity-linked effects, while mitigating genotype- and clone-specific biases[27].

Patient-derived somatic cells were reprogrammed into iPSC (2 mild, 2 moderate and 3 severe, two clones per patient), with sequencing confirming the presence of *LIS1* variants and comprehensive iPSC validation (Supplementary Fig. S1B–K, Supplementary Data S1). We then generated FB organoids[28] from the seven patient lines and the control iPSC pool.

To capture early progenitor disruptions caused by LIS1 dysfunction, we focused our analysis on day 23 ± 3 organoids, a stage enriched in NE and early RG populations. Control and mild LIS1-organoids formed regular NE loop-like structures, while moderate organoids were generally smaller, and severe ones showed irregular edges with cells protruding into the embedding matrix (Fig. 1B, Supplementary Fig. S2A). Immunohistochemical analysis revealed a prominent neuronal belt in severe organoids, less pronounced in mild and moderate, and nearly absent in controls (Fig. 1C, Supplementary Fig. S2B). Hematoxylin–eosin (HE) staining and structural analysis showed a progressive decline in VZ size and organization with increased severity: control organoids displayed compact, well-organized VZ loops, while moderate and severe samples had smaller, disorganized structures with reduced cellular density (Fig. 1D, Supplementary Fig. S2B, C). These data indicate that LIS1 mutations compromise VZ cytoarchitecture, potentially affecting progenitor maintenance and neurogenesis. To quantify severity-linked changes in VZ cytoarchitecture, we analyzed six morphological parameters: apical and basal membrane lengths, VZ diameter and size, and total loop area and size[9]. Severe cases differed significantly from controls in all six metrics, moderate cases in four, and mild cases in two. Pairwise comparisons revealed significant differences between mild and severe in five parameters and between moderate and severe in three parameters, indicating a progressive disruption of VZ architecture with increased disease severity (Fig. 1E, Supplementary Fig. S2D, Supplementary Data S2).

Single-cell transcriptomics reveal severity-linked progenitor disruption and stress signatures in LIS1-lissencephaly

To determine whether the observed structural changes correspond to molecular alterations in cell composition and progenitor behavior, we next performed single-cell RNA sequencing (scRNA-seq) on day 23 ± 2 organoids across all severity grades (two to three pooled organoids from two genetic backgrounds per condition; Fig. 1F–J). Based on

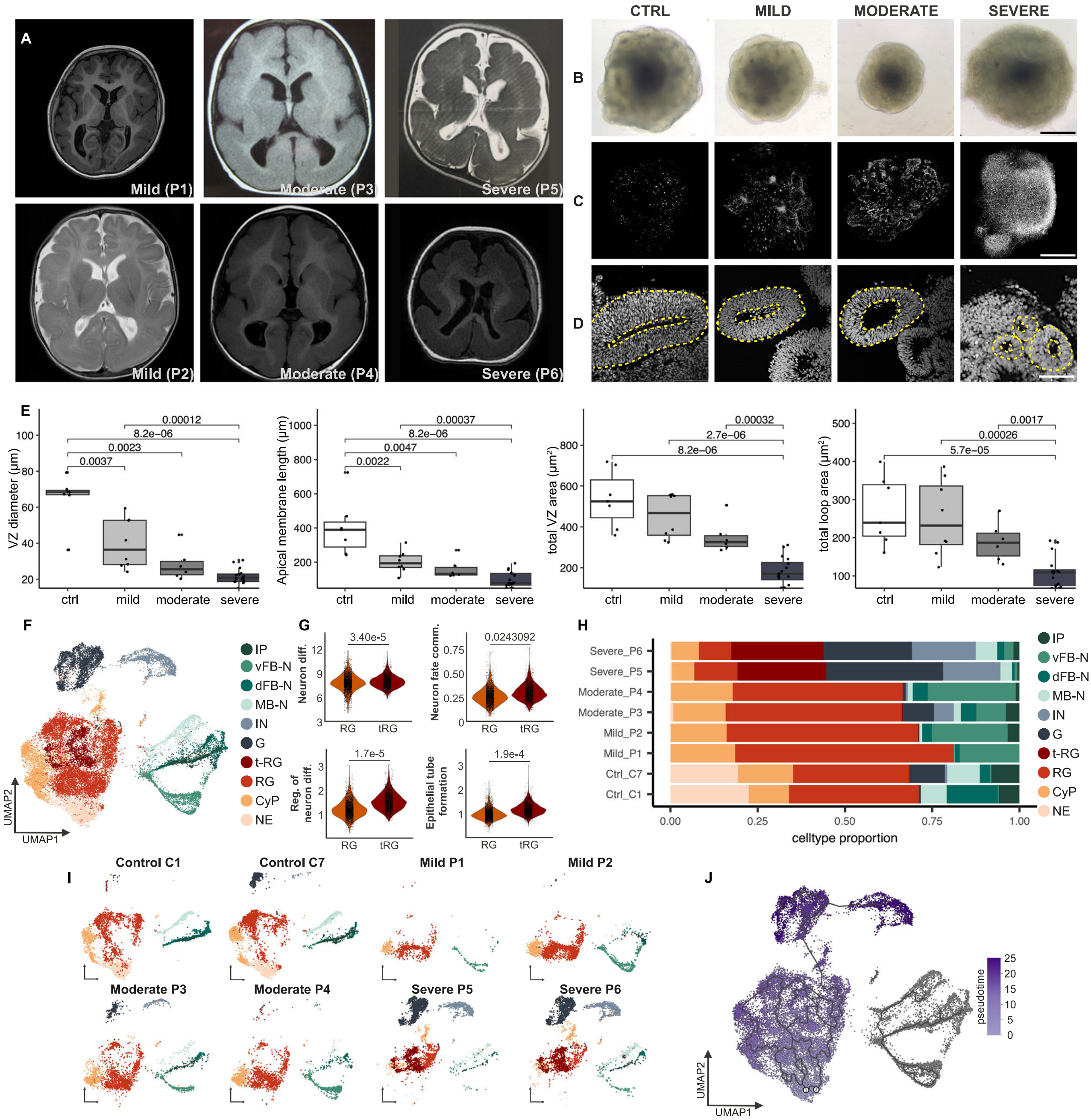

Fig. 1 | Morphological and cellular characterization of LIS1 patient-derived organoids across severity grades. A Representative MRI scans from patients with mild, moderate, and severe LIS1-lissencephaly reveal increasing cortical malformation severity. Mild cases show posterior pachygyria with preserved frontal regions; moderate cases display posterior pachygyria extending into the parietal and occipital lobes with mild frontal involvement; severe cases exhibit diffuse pachygyria or near-complete agyria, mainly in posterior regions. **B** Brightfield images of control and patient-derived organoids at day 20 demonstrate morphological changes correlating with severity. **C** Light sheet microscopy of whole-tissue cleared day 20 organoids, immunostained for β-III tubulin (TUBB3), shows differences in neuronal organization across severity grades. **D** Hoechst staining of ventricular zone (VZ) structures at day 20 reveals progressive disruption in VZ architecture with increasing disease severity. Yellow dotted lines delineate VZ boundaries. **E** Quantification of VZ structural parameters demonstrates significant differences among groups. Individual data points represent mean values from independent differentiations (control *n* = 7, mild *n* = 8, moderate *n* = 6, severe *n* = 16; ≥3 organoids and 8 VZs per differentiation; total VZs: control = 71, mild = 70, moderate = 63, severe = 222). Boxplots show median, 25th/75th percentiles, and 1.5 interquartile range whiskers, Kruskal–Wallis test with Wilcoxon post hoc correction. **F** UMAP dimensionality reduction and clustering identifies 10 distinct cell populations in day 23 ± 3 organoids: neuroepithelial cells (NE), cycling progenitors (CyP), radial glia (RG), intermediate progenitors (IP), transitory RG (t-RG), dorsal forebrain neurons (dFB-N), ventral forebrain neurons (vFB-N), midbrain neurons (MB-N), interneurons (IN), and astroglia progenitors (G). **G** Violin plots of GO term scores show differences between t-RG and RG populations (Wilcoxon test). **H** Cell type distributions by severity grade and sample. **I** UMAP plots split by individual samples. **J** UMAP depicting developmental trajectories from NE cells through RG to neuronal populations. Panels **F**–**J**: Analyses based on 23 organoids (control = 6, mild = 6, moderate = 5, severe = 6; two cell lines per condition), total 24,982 single cells. Scale bars: **B**, **C** 200 µm; **D** 50 µm. All statistical tests were performed as two-sided. Source data are provided as a Source Data file.

established markers[16,29,30], we identified nine major populations, including NE, cycling progenitors (CyP), RG, intermediate progenitors (IP), neurons from dorsal/ventral forebrain and midbrain (dFB-N, vFB-N, MB-N), interneurons (IN), and astroglial progenitors (G) (Fig. 1F; Supplementary Fig. S3A). In severe cases, we detected a unique transitional RG (t-RG) population co-expressing RG markers with early neuronal genes (t-RG; Fig. 1G, Supplementary Data S3).

Cell type proportion analysis showed a significant reduction in neural progenitors and increased IN and G, in severe LIS1-patient organoids (Fig. 2H, I; Supplementary Fig. S3B). Although scRNA-seq showed similar total neuronal proportions across groups, matched immunohistochemistry revealed increased neuronal marker expression (HuC/D, TUBB3, Supplementary Fig. S3C). This discrepancy was consistent across multiple differentiations (Fig. 1C; Supplementary Fig. S2B), suggesting selective loss of neurons during library preparation. Similarly, while scRNA-seq indicated increased astroglia progenitors and interneuron markers in severe samples, parallel immunostaining for S100ß and somatostatin (SST) did not confirm these changes at the protein level (Supplementary Fig. S3D), suggesting temporal differences between mRNA expression and protein translation. Progenitor profiling showed NE depletion in all patient groups. While RG cells increased in mild and moderate conditions, severe cases showed a clear reduction alongside t-RG emergence. These shifts suggest a premature NE-to-RG-to-neuron transition. Pseudotime analysis confirmed this trajectory (Fig. 1J). GO enrichment of apoptosis-related genes indicated no pathway-level enrichment, supporting differentiation over cell death as the main driver of NE loss (Supplementary Fig. S3E).

To uncover shared and severity-linked progressive molecular changes, we performed differential expression analysis in the pooled progenitor cell types (NE, RG, t-RG), excluding cycling progenitors, to avoid cell cycle bias. This identified 140 significantly differentially expressed (DE) genes in mild, 80 in moderate, and 104 in severe samples compared to controls. (Supplementary Datas S4–S7). We found 29 genes commonly deregulated across all severity levels, along with uniquely overlapping subsets between mild and moderate (28), moderate and severe (12), and mild and severe (9), reflecting both converging and distinct molecular signatures across the LIS1 spectrum (Fig. 2A, B, Supplementary Datas S4–S7). Among the 29 core DE genes shared across all LIS1 conditions were several with established roles in neurodevelopment and signaling, including *DLK1* (a Notch ligand marking NE to RG transition[31]), the transcription factors *FOXG1*, *LHX2*, and *NR2F1* (regulators of early cortical patterning and NE identity[32,33]); and *SFRP1* and *WLS* (key WNT modulators influencing progenitor fate and cortical expansion[34,35]). Stress- and metabolism-related genes (*CLU*, *MTRNR2L8*, *MTRNR2L12*) were also consistently deregulated, suggesting mitochondrial stress and proteostasis imbalance[36,37] (Fig. 2A, B; Supplementary Data S7). Each severity grade showed distinct transcriptional signatures: *FZD5* (a WNT receptor involved in anterior-posterior patterning[38]) was highly upregulated in mild organoids; *LIX1*, enriched in early RG and linked to progenitor dynamics[39], in moderate; and *SRP14*, involved in endoplasmic reticulum (ER) targeting and stress buffering[40], in severe (Supplementary Data S7). Several gene changes were shared between specific severity pairs. Mild and moderate samples co-deregulated WNT-related genes, including *FZD8*[41]; moderate and severe shared stress and translational regulators, such as *NNAT*[42]; and mild and severe shared neurodevelopmental genes like *FGFBP3* and *EMX2*[43,44]. Mitochondrial DE genes (*NDUFB11*, *MT-ND3*, *NDUFA1*, *ATP5ME*) were shared across mild and severe conditions, pointing to a common mitochondrial stress axis[45] (Supplementary Data S7). Together, these data highlight converging and diverging molecular alterations in developmental signaling, stress response, and mitochondrial function across the LIS1-lissencephaly severity spectrum.

Proteomic analyses identify LIS1 protein dosage changes and severity-linked co-regulated modules

To investigate molecular mechanisms underlying LIS1-lissencephaly severity, we generated homogeneous cortical progenitor cultures from control, mild, moderate, and severe LIS1 patient iPSC[9,46] and quantified protein abundances using label-free mass spectrometry (2 lines per condition, control and mild: $n = 4$ each; moderate and severe: $n = 6$ each, Supplementary Fig. S3F). TUBB3 staining after growth factor withdrawal confirmed increased neurogenesis with severity (Supplementary Fig. S3G), while Caspase-3 staining revealed no increase in apoptosis (Supplementary Fig. S3H), consistent with transcriptional findings.

Proteomic comparison identified 67, 157, and 542 DE proteins before adjusting for multiple testing in mild, moderate, and severe organoids, respectively (Fig. 2C, Supplementary Data S8). LIS1 protein levels declined progressively with severity, showing significant reduction in moderate ($r = -0.81$, $p = 0.01$) and severe ($r = -0.81$, $p = 0.01$) compared to control, and between mild and moderate ($r = 0.81$, $p = 0.01$) as well as mild and severe ($r = -0.81$, $p = 0.01$). Although patients in the severe group were more clinically affected, and their organoids exhibited more pronounced phenotypic alterations (Fig. 1), LIS1 protein levels in their progenitor cells were slightly higher than in the moderate group. LIS1 transcript levels showed an inverse pattern, suggesting post-transcriptional regulation. We also detected severity-linked dysregulation of several LIS1-interacting proteins (e.g., FUS, SRSF1, GSP90, SSB, DYNC1H1, TUBB), supporting altered LIS1 function (Fig. 2D). Unbiased network analysis (WGCNA) revealed two severity-associated protein modules (Fig. 2E). The turquoise module, consistently downregulated, was enriched for proteasomal and translational machinery (Supplementary Fig. S3J; Supplementary Data S9), implicating global proteostasis impairment. The blue module, progressively downregulated with severity, was enriched for RNA splicing, cadherin binding, and unfolded protein binding (UPB, Fig. 2E Supplementary Data S9). Subnetwork analysis revealed clusters of splicing regulators (e.g., NCL and DDX3X), ribosome assembly, translation factors, and ER stress chaperones (e.g., BiP, HSP90) (Fig. 2F). As ER stress-related genes also emerged from our transcriptomic analyses (Supplementary Datas S4–S7), and given the established link between ER stress, unfolded protein response (UPR) and neurogenic timing[47], we further investigated this pathway. Immunohistochemistry revealed severity-dependent changes in stress-related proteins, with increased HSP90 expression across all patient groups and elevated BiP in moderate and severe organoids (Fig. 2G). Additionally, we noted distinct expression changes in select proteins linked to mitochondrial and stress pathways across severity grades (Supplementary Fig. S3K), further confirming persistent cellular stress that parallels the premature neuronal differentiation phenotype (Fig. 1C, Supplementary Fig. S2B).

Together, these findings highlight functional LIS1 dosage, rather than protein abundance alone, as a critical determinant of disease severity and establish ER stress as a convergent mechanism in LIS1-lissencephaly.

Integrative analysis of differential RNA and protein regulation identified critical severity grade-dependent phenotypes in LIS1-patient organoids

To investigate how LIS1 dysfunction affects neurodevelopmental pathways across severity levels, we performed integrative gene ontology (GO) enrichment analysis combining transcriptomic and proteomic data. This revealed severity-linked alterations in cortical development processes, including FB specification, progenitor proliferation, and neurogenesis (Fig. 2H, Supplementary Fig. S3L, full results Supplementary Data S10, S11). Many categories showed severity-linked gradients, especially at the RNA level across all LIS1 groups, and at the protein level in moderate and severe cases. We also

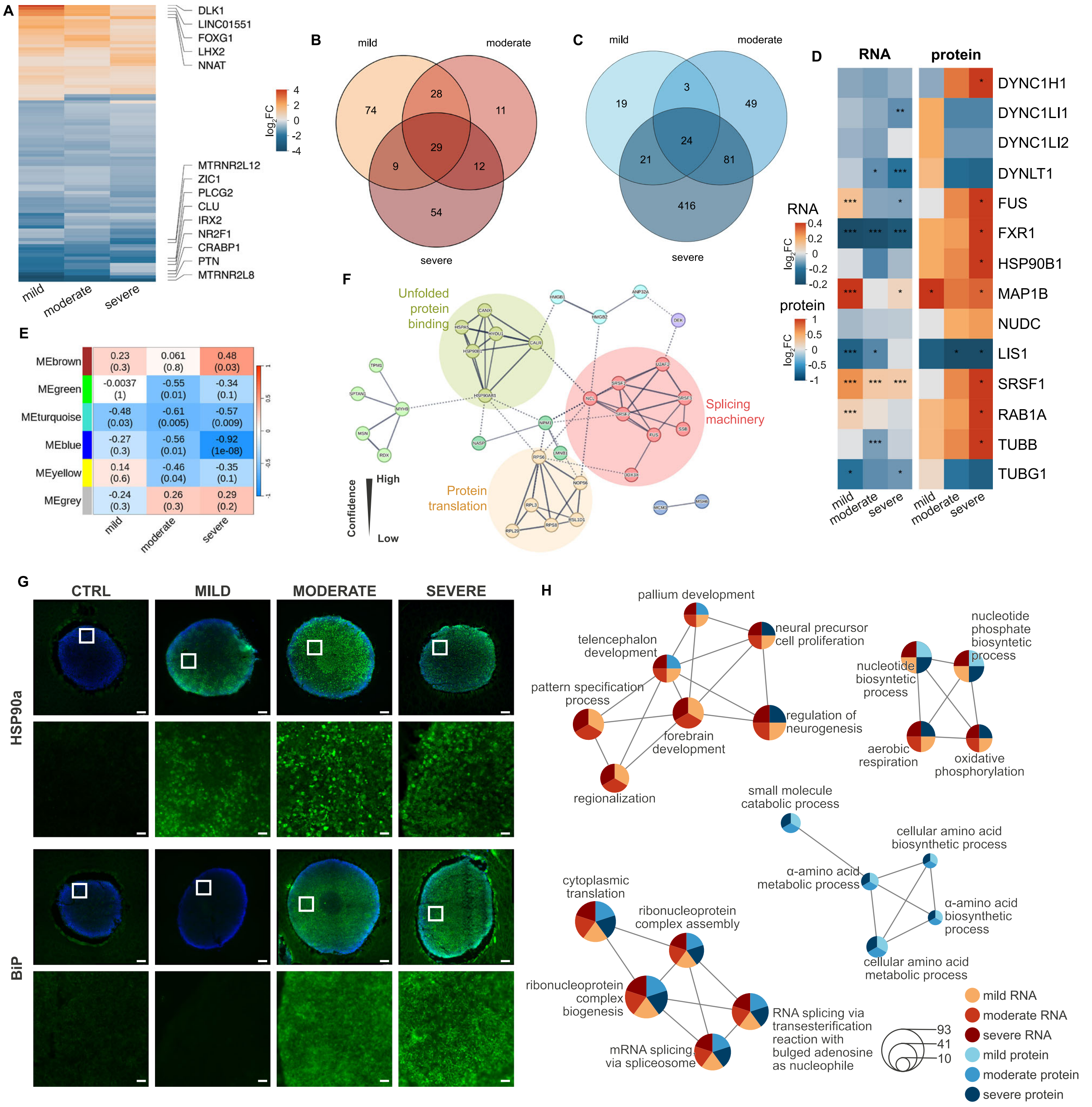

Fig. 2 | Transcriptomic and proteomic dysregulation in LIS1 patient-derived organoids across severity grades. **A** Heatmap showing differentially expressed genes between control and mild, moderate, and severe LIS1-lissencephaly grades for genes expressed in all conditions (adjusted $p < 0.05$; $|\log_2\text{FC}| > 0.5$). Top 10 genes with the largest absolute $\log_2$FC per condition are annotated, where present in all three severity grades. Color intensity represents $\log_2$FC. **B** Venn diagram showing overlap of differentially expressed genes between mild, moderate, severe, and control groups. **C** Venn diagram illustrating overlap of differentially expressed proteins among the same groups. **D** Heatmap displaying $\log_2$FC (RNA) and Wilcoxon's *r* (protein) for LIS1 and its interaction partners between severity grades and control. **E** Heatmap depicting the correlations of module eigengenes from WGCNA modules and severity grades. **F** STRING network of proteins in the WGCNA blue module, clustered by MCL (inflation parameter = 3). Only high-confidence interactions (score ≥ 0.700) are shown. **G** Representative widefield images of day 18 control and patient-derived organoids stained for HSP90α and BiP, counterstained with DAPI. White squares mark higher-magnification regions. **H** Map plot of overrepresented GO biological processes in differentially regulated genes and proteins; circle size indicates the number of features in each GO term. **A**, **B**, **D**, **G**, **H**: day 23 ± 3 organoids. Organoids analyzed: 23 total (control *n* = 6, mild *n* = 6, moderate *n* = 5, severe *n* = 6; two cell lines per condition). Single cells: control 8647; mild 3444; moderate 5168; severe 7723. **C**–**F**, **H**: 2 independent lines per condition; control and mild: 4 samples each; moderate and severe: 6 samples each. Scale bars: **G** overviews 100 µm, details 20 µm. All statistical tests were performed as two-sided. Source data are provided as a Source Data file.

found consistent enrichment across conditions in pathways related to RNA splicing, translation, and energy metabolism, indicating broad cellular disruption (Supplementary Data S10, S11).

Focusing on molecular function terms, we noted enrichment in categories linked to tubulin-, actin-, cadherin-, and WNT-protein binding (Supplementary Fig. S3K, Supplementary Data S11). Cytoskeleton-related terms showed progressive deregulation, particularly actin binding, actin filament organization, and overall cytoskeletal structural integrity at the protein level. Tubulin binding was enriched explicitly in severe cases at the protein level (Fig. 3A),

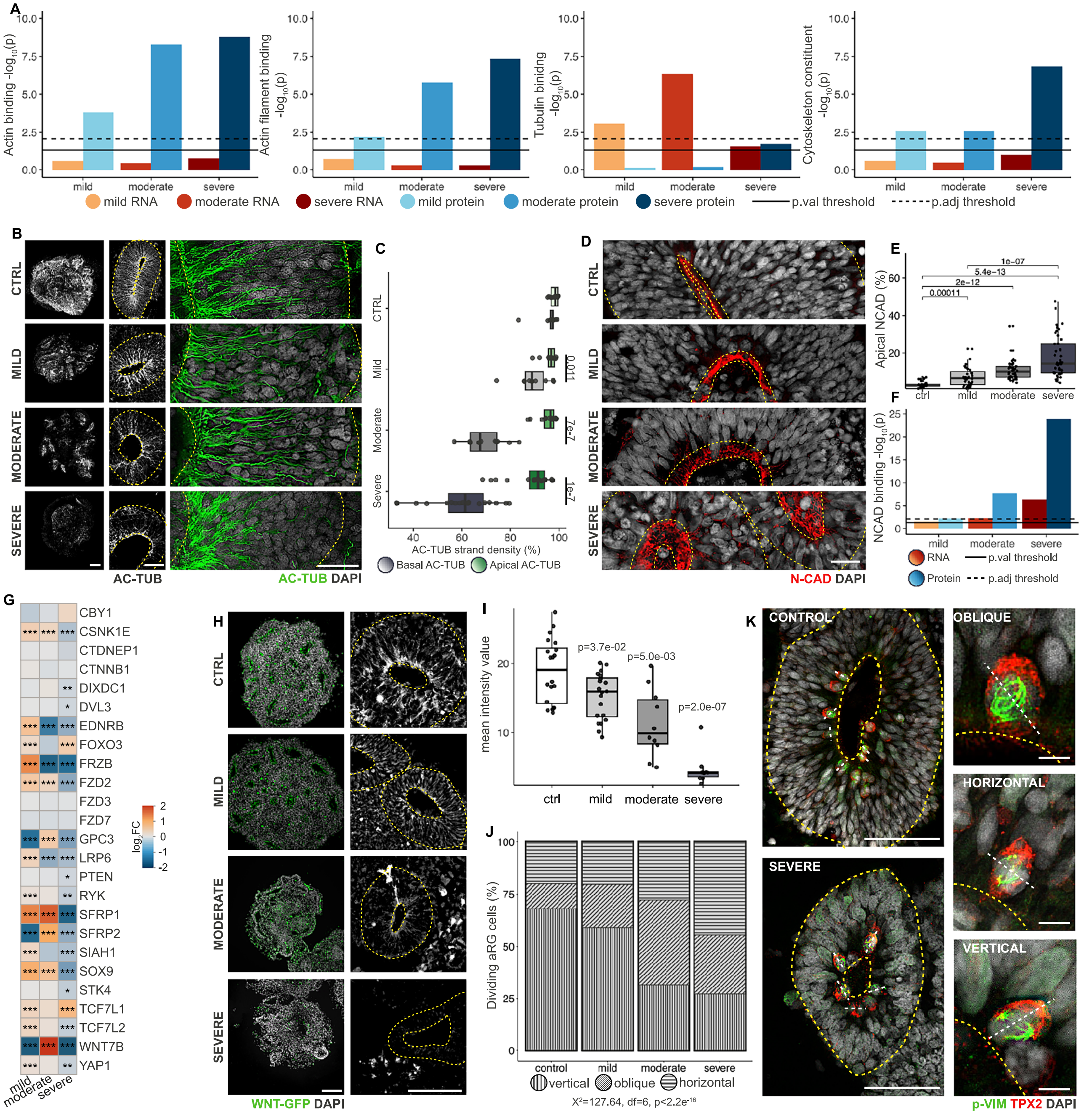

Fig. 3 | Probing selective molecular pathways identified in the OMICS analyses in LIS1-pateint-derived organoids. **A** Bar graphs of $-\log_{10}$-transformed p-values from GO molecular function enrichment for actin binding, actin filament binding, tubulin binding, and cytoskeleton structural constituent; nominal significance $p = 0.05$; p-value adjusted with Bonferroni correction; two-sided Hypergeometric test. **B** Representative day 20 organoids stained for acetylated α-tubulin (Ac-TUB); yellow dashed lines, apical/basal VZ regions. **C** Quantification of Ac-TUB strand density at day 20: $n = 11$ control (4 cell lines), 10 mild, 12 moderate, 18 severe (2 cell lines each), across four differentiations. VZ loops: 41, 54, 49, 80, respectively; two-sided Wilcoxon test. **D** Day 20 organoids stained for N-cadherin (N-CAD); yellow dashed lines, VZ edges and N-cadherin diameter expansion. **E** Quantification of apical N-CAD signal at day 20: VZ structures $n = 32$ control, 39 mild, 42 moderate, 43 severe for a total of 6, 8, 7, and 9 differentiations, respectively; 2 cell lines each; two-sided Kruskal–Wallis with post hoc Wilcoxon correction. **F** GO enrichment for cadherin binding; nominal significance $p = 0.05$; p-value adjusted with Bonferroni correction; two-sided Hypergeometric test. **G** Heatmap of $\log_2$FC for WNT pathway genes in cycling progenitors by severity grade versus control ($^*P < 0.05$, $^{**}P < 0.01$, $^{***}P < 0.001$); two-sided Wilcoxon test. **H** WNT-GFP reporter organoids at day 20; yellow dashed lines, VZ boundaries. **I** Mean value of WNT-GFP intensity per VZ: $n = 20$ control (2 cell lines), 20 mild (2 cell lines), 10 moderate (one cell line), 10 severe (one cell line); 3 organoids per condition from two differentiations per cell line; two-sided Kruskal–Wallis with post hoc Wilcoxon correction. **J** Quantification of cell division plane orientation: $n = 13$ control, 12 mild, 12 moderate, 15 severe. VZ loops: 59, 56, 43, 57; cells: 206, 359, 172, 249, respectively; Chi-square test. **K** Examples of division planes in control and severe organoids; yellow dashed lines, VZ edges; white dashed lines, division plane orientation. Scale bars: **B** left 200 μm, **B** right, **H** 50 μm; **D**, **K** 20 μm; All boxplots show median, 25th/75th percentiles, and 1.5 interquartile range whiskers. Source data are provided as a Source Data file.

suggesting increased microtubule destabilization with severity. To validate these findings, we analyzed microtubule architecture by immunolabeling for acetylated alpha-tubulin (Ac-TUB), a marker of microtubule stability. Tissue clearing and whole-organoid staining revealed a global reduction of Ac-TUB-positive fibers in LIS1 organoids, with severity-linked loss (Fig. 3B). In contrast to control organoids, patient-derived organoids showed a significant depletion of basal strands, most prominent in severe cases (Fig. 3B, C, Supplementary Data S12). Pairwise comparisons confirmed significant differences between controls and each severity group and between all severity grades (mild vs. moderate, mild vs. severe, and moderate vs. severe, Fig. 3C, Supplementary Data S12). These results identify microtubule destabilization in RG processes as a core structural phenotype in LIS1-lissencephaly that correlates with clinical severity and likely reflects increasing impairment of LIS1-mediated microtubule regulation.

Given LIS1´s established role in microtubule regulation and its contribution to apico-basal polarity and adherens junctions[9,48], we next assessed N-cadherin distribution. We observed a clear severity-linked gradient of N-cadherin mislocalization across patient-derived organoids (Fig. 3D–F, Supplementary Data S13). In control organoids, N-cadherin was tightly confined to the apical surface, whereas in LIS1 organoids, its signal became progressively broader and more dispersed from mild to severe conditions. Quantitative analysis confirmed significant differences relative to controls and between all severity groups (mild-moderate, mild-severe, and moderate-severe; Fig. 3E). This identifies N-cadherin mislocalisation as a progressive molecular marker of LIS1 dysfunction. Supporting this, GO term analysis revealed a severity-linked increase in cadherin-binding proteins at both RNA and protein levels, with the strongest enrichment in severe cases (Fig. 3F). Together, these findings implicate compromised adherens junction integrity as a key pathological feature contributing to VZ disorganization and cortical malformation in LIS1-lissencephaly.

Adherens junctions regulate ß-catenin mediated WNT signaling, essential for RG proliferation and fate decisions[49,50]. Our prior study in MDS organoids has shown that LIS1 modulates WNT signaling via N-cadherin integrity[9]. Consistent with this, our scRNA-seq analysis revealed severity-linked dysregulation of WNT-related genes (Fig. 2A, B, Supplementary Data S4–S7). GO analysis supported progressive WNT pathway disruption (Supplementary Fig. S3K). Stratified analysis within CyP populations confirmed increasing WNT-associated transcripts dysregulation with severity (Fig. 3G). To assess pathway activity, we used WNT-GFP iPSC reporter organoids and found a severity-correlated reduction in apical WNT activity (Fig. 3H, I). Since impaired WNT promotes premature neurogenesis via altered RG division modes[9], we analyzed mitotic spindle orientation and observed increased horizontal and oblique divisions, especially in severe LIS1 organoids (Fig. 3J, K). These findings indicate that LIS1 dysfunction disrupts WNT signaling at both transcriptional and functional levels, contributing to premature neurogenesis and progenitor pool depletion.

Across multiple independent patient-derived lines, we observed a severity-linked reduction in acetylated tubulin, progressive N-cadherin mislocalization, and decreased WNT pathway activity. These phenotypes scale with clinical severity but do not strictly correlate with LIS1 protein levels. Consistent with our prior rescue experiments in MDS[9] linking LIS1 to these pathways, our findings demonstrate that disruptions in microtubule integrity, adherens junctions, and WNT signaling extend across genetically distinct *LIS1* mutations and reflect both reduced protein dosage and mutation-specific dysfunction.

Pharmacological rescue of cellular phenotypes in LIS1-patient-derived organoids

Our data identify three mechanistically distinct but converging pathways disrupted in LIS1-lissencephaly: microtubule destabilization, impaired WNT signaling, and proteostasis dysregulation, each showing severity-linked gradients. To assess whether these pathways causally contribute to observed phenotypes and are amenable to intervention, we performed targeted pharmacological rescue experiments in LIS1-patient organoids.

We treated organoids from day 10 to 15 (a critical window for progenitor organization) with EpoD, a microtubule-stabilizing macrolide[21]), and CHIR99021, a GSK3ß inhibitor that activates WNT signaling[22]. EpoD treatment partially restored Ac-TUB strand density, apical N-cadherin localization, and VZ morphology in severe-grade organoids (Fig. 4A–C, Supplementary Fig. S4A, B, Supplementary Data S14–16), and reduced neuronal belt size, indicating mitigation of premature neurogenesis (Supplementary Fig. S4C). Effects were less prominent in mild and moderate samples and absent in controls, indicating specificity for LIS1-related defects. CHIR99021 similarly improved VZ structures and reduced neuronal belts, with the strongest effects in severe-grade organoids (Fig. 4D, Supplementary Fig. S4D, E, Supplementary Data S15). Importantly, it rescued aberrant mitotic spindle orientation in severe cases (Fig. 4E, Supplementary Data S17), suggesting restored progenitor behavior. Improvements across LIS1 samples, but not controls, further support specificity for LIS1-related WNT disruption. Given the known role of WNT signaling in brain organoid regional patterning[51] and progenitor dynamics during early brain organoid development[35], prolonged treatment with these compounds is likely to perturb normal developmental trajectories, supporting the rationale for short-term interventions. These results underscore the importance of timing and dosage, highlighting that stage-specific interventions may effectively restore progenitor organization in LIS1-lissencephaly

To evaluate the functional relevance of proteostasis disruption in LIS1-lissencephaly and its contribution to premature neurogenesis, we performed in silico drug repurposing using the Connectivity Map (CMap) to compare the transcriptional profile of LIS1-RG cells against a database of compound-induced signatures. This analysis identified mTOR inhibition as the top-enriched mode of action, with Everolimus, emerging as a leading candidate (Fig. 4F, G). Everolimus selectively inhibits mTORC1, a nutrient- and stress-sensitive kinase complex, reducing protein synthesis and alleviating ER stress from misfolded protein accumulation[23]. When administered to LIS1-patient organoids from day 10 to 19, a critical window for progenitor maintenance, Everolimus significantly reduced premature neurogenesis (Fig. 4H, Supplementary Fig. S4F, Supplementary Data S18), and lowered expression levels of ER stress markers, including GRP170 (HYOU1), and BiP (HSPA5), particularly in moderate and severe cases (Fig. 4I, J).

These findings validate mTOR-mediated proteostasis disruption as a contributor to LIS1-lissencephaly and highlight that microtubule stabilization, WNT pathway activation, and proteostasis modulation affect progenitor maintenance via distinct molecular routes.

Severity-linked progenitor phenotypes persist in LIS1-patient-derived neuronal populations

To assess whether disease-associated mechanisms persist beyond early progenitor stages, we performed scRNA-seq on day 60 ± 3 organoids (three pooled organoids per condition from two genetic backgrounds for control and severe, and one for mild and moderate). We identified nine major cell types based on established marker genes[16,29,30], including RG, bRG, extracellular matrix-enriched progenitors (ECM-P), stressed progenitors (SP), intermediate progenitors (IP), early-born neurons (EBN), excitatory neurons (EN), interneurons (IN), and stressed neurons (SN) (Fig. 5A, Supplementary Fig. S5A).

Overall, progenitor to neuron distribution remained largely stable across conditions. However, we observed two severity-linked neuronal trends: reduced EN across all LIS1-patient samples and increased SN abundance in moderate and severe cases. In contrast to earlier stages, IN proportions did not show consistent enrichment in severe conditions (Fig. 5B).

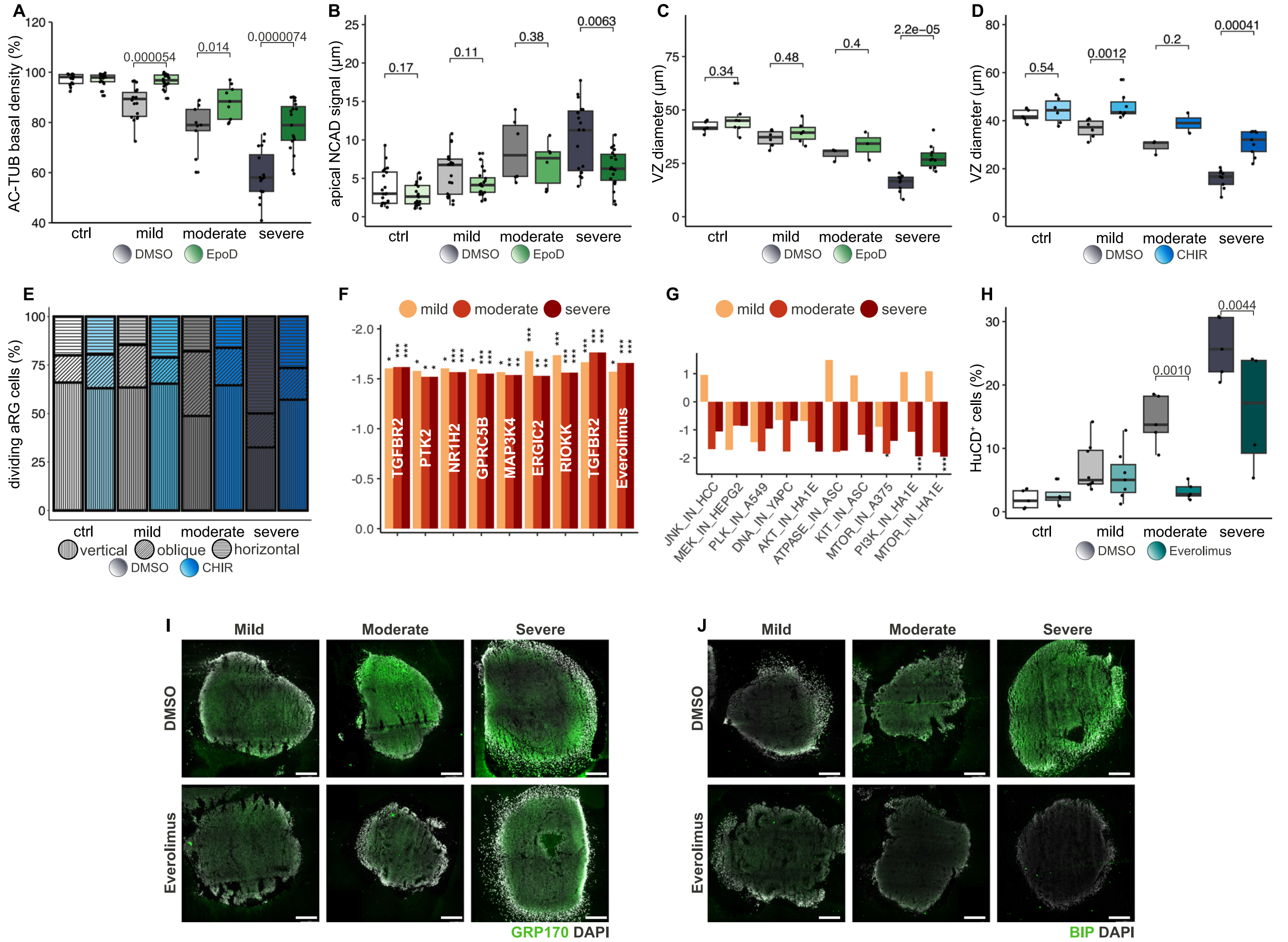

Fig. 4 | Probing therapeutic targets in LIS1 patient-derived organoids. **A** Basal Ac-TUB strand density in DMSO- or EpoD-treated day 15 organoids. *n* = 6 organoids/group (3 moderate); VZs = 18/group (9 moderate), two differentiations/group, two genetic backgrounds (one moderate). Kruskal–Wallis with post hoc Wilcoxon. **B** N-CAD diameter in day 15 DMSO/EpoD-treated organoids. Each dot represents a VZ structure: 20 control, 20 mild, 6 moderate, 19 severe (6, 6, 3, 9 differentiations, respectively; two genetic backgrounds/conditions), pairwise Wilcoxon test. **C** VZ diameter on day 15 DMSO- and EpoD-treated control and LIS1-organoids. Each dot shows the mean of one differentiation: control DMSO = 5 organoids, EpoD = 7; mild DMSO = 6, EpoD = 6; moderate DMSO = 3, EpoD = 3; severe DMSO = 9, EpoD = 10. VZ: control DMSO = 27, EpoD = 39; mild DMSO = 28, EpoD = 24; moderate DMSO = 14, EpoD = 11; severe DMSO = 41, EpoD = 41. **D** VZ diameter on day 15 DMSO- and CHIR-treated organoids. Each dot indicates the mean of one differentiation: control DMSO = 7 organoids, CHIR = 6; mild DMSO = 6, CHIR = 7; moderate DMSO = 3, CHIR = 2; severe DMSO = 9, CHIR = 9. VZ: control DMSO = 27, CHIR = 38; mild DMSO = 28, CHIR = 23; moderate DMSO = 14, CHIR = 13; severe DMSO = 41, CHIR = 38; pairwise Wilcoxon test. **E** Cell division plane orientation in DMSO/CHIR-treated organoids. *n* = 6 organoids/group, 9 VZs/group; dividing cells: *n* = 50 control DMSO, 46 CHIR; 41 mild DMSO, 52 CHIR; 39 moderate DMSO, 31 CHIR; 40 severe DMSO, 49 CHIR; Chi square test. **F** and **G** Connectivity scores from CMap analysis for perturbagen classes (**F**) and modes of action (**G**) across severity groups; $^{*}P < 0.05$, $^{**}P < 0.01$, $^{***}P < 0.001$; individual *p* values are provided in Supplementary Data S24 (**F**) and S25 (**G**); Kolmogorov–Smirnov statistic vs. random query null distribution, as implemented by clue.io. **H** HuCD+ cells in DMSO/everolimus-treated organoids at day 20; differentiations: *n* = 4 control, 8 mild, 5 moderate, 4 severe; organoids: *n* = 19 control, 29 mild, 26 moderate, 28 severe; 2-way ANOVA with Bonferroni correction. **I** and **J** Representative images of organoids stained for GRP170 (**I**) and BiP (**J**) after everolimus. Scale bars: 125 µm. All statistical tests were performed as two-sided unless the Chi-square test. All boxplots show median, 25th/75th percentiles, and 1.5 interquartile range whiskers. Source data are provided as a Source Data file.

To investigate cytoskeleton dysregulation in neurons, we performed GO and KEGG enrichment analyses on neurons from severe vs. control organoids. We focused on the severe group, as these organoids exhibited the most pronounced alterations across all investigated pathways during early development. As expected from LIS1´s role in cytoskeletal regulation, we found significant enrichment for microtubule-related processes, axonogenesis, and cytoskeletal remodeling (Fig. 5C). Immunohistochemistry on day 58 ± 2 organoids confirmed hallmarks of LIS1-lissencephaly pathology. Control samples display well-organized VZ and distinct NLs, with clear expression of TBR1, CTIP2, and SATB2. In contrast, LIS1-patient organoids exhibited smaller VZ loops and a diffuse distribution of NL markers throughout the tissue (Fig. 5D), indicating disrupted lamination and impaired neuronal migration. These findings confirm that cytoskeletal and neuroarchitectural defects persist into later-stage LIS1 organoids.

Having established that our model recapitulates known LIS1-related neuronal defects in severe derived organoids at both the transcriptomic and cellular levels, we next asked whether the identified mechanisms—particularly proteostasis dysregulation—also persist in severe derived neurons. We performed DE, GO, and KEGG analyses on pooled neuronal clusters (excluding but also specifically analyzing the SN cluster to control for stress bias). This analysis revealed upregulation of chaperone-related genes, including HSPA5 (BiP), DNAJB1, PPIB, and HSP90B1[52], and significant enrichment of 12 and 22 GO/KEGG categories, in pooled and SN neurons, respectively, associated with protein folding, ER stress, and reactive oxygen species metabolism (Fig. 5E, F, Supplementary Fig. S5B, C). These findings suggest that proteostasis stress is a persistent feature of the severe LIS1 condition, extending beyond early progenitor cells into differentiated neurons.

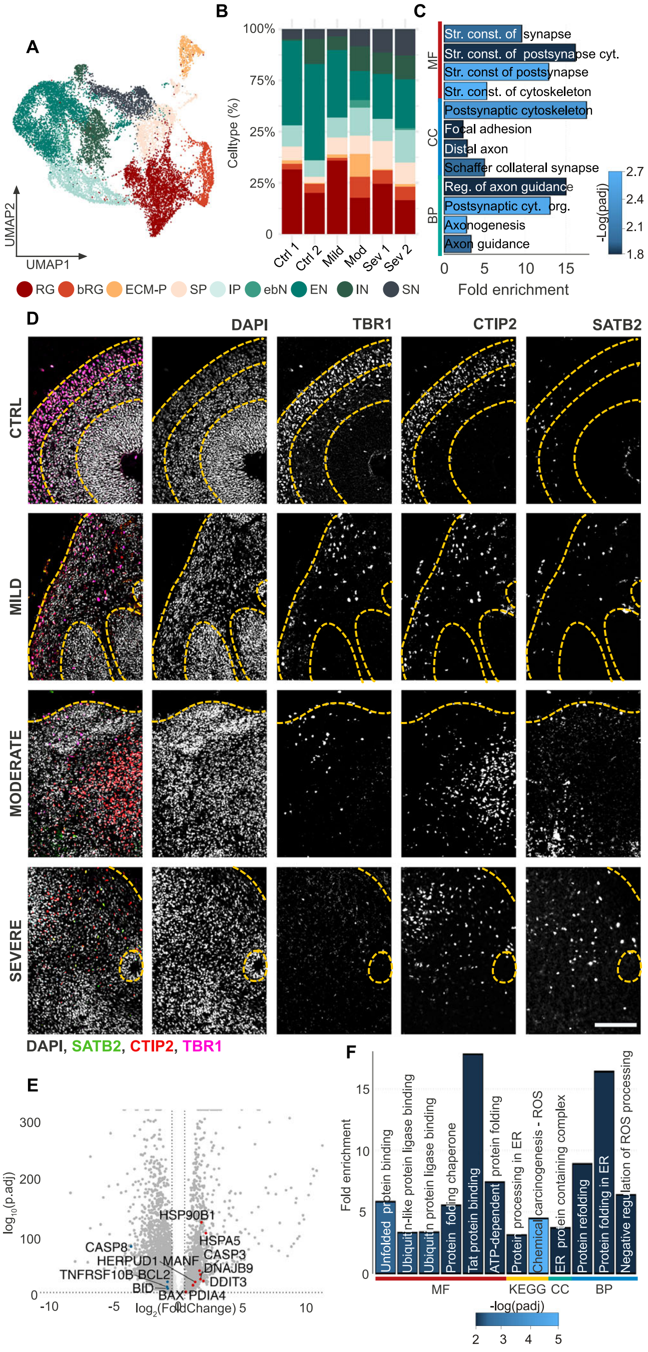

Fig. 5 | Transcriptomic dysregulation in neurons of late-stage LIS1 patient-derived organoids. A UMAP dimensional reduction and unbiased clustering reveal 9 distinct color-coded cell populations within control, mild-, moderate- and severe LIS1 patient-derived organoids: RG, basal radial glia (bRG), extracellular matrix-enriched progenitors (ECM-P), stressed progenitors (SP), intermediate progenitors (IP), early-born neurons (ebN), excitatory neurons (EN), interneurons (IN) and stressed neurons (SN). **B** Cell type distribution in each severity grade, divided by sample. **C** GO enrichment of cytoskeleton-, synaptic- and axon-related terms among genes with log2FC > 0.5 (adj. $p < 0.05$) in the pooled neuronal clusters excluding the SN, showing fold-enrichment for biological processes (BP), molecular function (MF) and cellular components (CC). Fisher's exact test with Benjamini–Hochberg correction. **D** Representative stainings of day 58 ± 2 control, mild, moderate and severe grade patient-derived organoids for the cortical layer specific markers TBR1, CTIP2 and SATB2 counterstained with Hoechst. The yellow dotted lines indicate the basal edges of the VZ, the blue dotted lines those of the NL regions. **E** Volcano plot of differential expression in the pooled neuronal clusters excluding the SN (severe vs. control), with stress-related genes highlighted. Statistical test: two-sided Wilcoxon Rank Sum test, with Benjamini–Hochberg correction. **F** GO and KEGG enrichment of stress-related terms among genes with log2FC > 0.5 (adj. $p < 0.05$) in the pooled neuronal clusters excluding the SN, showing fold-enrichment for biological processes (BP), molecular function (MF), cellular components (CC) and KEGG categories. Statistical test: Fisher's exact test with Benjamini–Hochberg correction. Number of organoids and cells analyzed: 23 organoids, control $N = 6$, mild $N = 3$, moderate $N = 3$, severe $N = 6$ (cell lines per condition: 2 controls (5560 single cells), 1 LIS1 mild (1410 single cells), 1 LIS1 moderate (3925 single cells) and 2 LIS1 severe (5914 single cells). **A**–**C**, **E**, **F**: day 60 ± 3 organoids. All statistical tests were performed as two-sided. Scale bars 50 μm.

We also found dysregulated pathways linked to synaptogenesis and focal adhesion (Fig. 5C), implicating sustained adhesion-related defects that may impact synaptic development, consistent with the established role of cell adhesion molecules in synaptogenesis[53]. In contrast, WNT signaling alterations were not detected in neuronal clusters at the gene or pathway level (Supplementary Data S19–S21), indicating that WNT dysregulation is likely confined to early NE and RG stages.

Together, these findings show that while WNT signaling alterations are restricted to early progenitors, key defects in cytoskeletal integrity, proteostasis, and adhesion persist in LIS1-mutant neurons, highlighting their relevance for later neurodevelopmental stages.

Discussion

Our study provides mechanistic insights into the molecular underpinnings of LIS1-lissencephaly by modeling a clinically stratified spectrum of disease severity using patient-derived FB organoids. By integrating cytoarchitectural, transcriptomic, and proteomic data, we identify severity-linked alterations in progenitor homeostasis, neurogenesis, and neuronal development—revealing both shared and progressive features across different LIS1 mutations. These findings support an integrated model where microtubule destabilization, adherens junction disorganization, and impaired WNT signaling act as interconnected contributors to LIS1 pathology. Importantly, we uncover proteostasis dysregulation, including ER stress and UPR activation, as a previously unrecognized mechanism. These alterations follow a severity-linked gradient and persist from progenitors into later-stage neurons, indicating lasting disruption across developmental stages.

A key early finding across all patient-derived organoids was the depletion of NE cells, the earliest cortical progenitors that generate RG and early-born neurons[20]. Pseudotime analysis revealed a developmental trajectory from NE to RG and neuronal fates, suggesting a premature NE-to-RG transition in patient samples. Supporting this, apoptosis-related markers were not significantly enriched, indicating that progenitor loss is driven by accelerated differentiation, rather than cell death, in line with our previous observations in MDS organoids[9]. Supporting this, genes involved in early progenitor transitions were dysregulated: *DLK1*, a marker of NE-to-RG transition[31], was consistently altered across all grades, while *LIX1*, enriched in early RG and implicated in progenitor dynamics[39], was upregulated in moderate cases. These results highlight a shared early mechanism whereby LIS1 dysfunction promotes premature NE-to-RG transition. Given the foundational role of NE cells in cortical expansion[20], their depletion likely contributes to reduced cortical thickness in LIS1-lissencephaly[2,3]. Altogether, our findings emphasize that progenitor dysregulation in LIS1-lissencephaly begins at the earliest developmental stages of cortical development and is not limited to later defects in RG/bRG behavior or neuronal migration[7,8,18,19].

Notably, we observed a discrepancy between premature neuronal differentiation observed by immunohistochemistry and the neuronal proportion captured by scRNA-seq. We hypothesize that this inconsistency stems from the selective loss of immature neurons during tissue dissociation, as these cells are particularly sensitive to stress-induced apoptosis[54]. This vulnerability may be amplified in severe LIS1 organoids, where later-stage analyses revealed elevated ER stress and proteostasis disruption in neurons, suggesting increased susceptibility to dissociation-induced loss. In addition, our scRNA-seq analysis showed transient increases in gliogenic and interneuron populations in severe LIS1 organoids. These shifts were not sustained at later stages, likely reflecting disrupted progenitor identity and fate decision, potentially driven by upstream cytoskeletal and signaling abnormalities.

Given that NE cells give rise to RG[20], and that RG polarity is governed by cytoskeletal and junctional integrity[49,50], we examined whether differences in LIS1 dosage, as suggested[12,13], are associated with changes in these features. We observed a graded reduction in LIS1 protein levels across severity groups, but the correlation with phenotypic severity was non-linear: severe cases showed more pronounced microtubule-related disruptions despite slightly higher LIS1 levels than moderate cases. This suggests that protein abundance alone may not fully explain disease progression. Since LIS1 functions as a homodimer[5,6], mutations in severe cases may yield a structurally altered or dysfunctional protein that interferes with wild-type LIS1, consistent with a dominant-negative mechanism.

One central pathway disrupted in LIS1-lissencephaly links LIS1-dependent microtubule stability to N-cadherin localization, ß-catenin-mediated WNT signaling, and neurogenic output—a cascade we previously described in MDS-derived organoids using an isogenic LIS1 rescue model[9]. The current study extends this framework by modeling a graded, severity-linked loss of LIS1 function. At the root of this cascade is LIS1's role in dynein-mediated microtubule transport[5,6]. We show that microtubule destabilization—evidenced by reduced acetylated tubulin—is an early and severity-correlated phenotype that aligns with clinical severity and, in part, the graded reduction of LIS1-protein and perturbation of DYNC subunits. This cytoskeletal instability leads to progressively impaired N-cadherin localization at adherens junctions, weakening VZ architecture, and disrupted WNT signaling in a severity-linked manner, as confirmed using WNT-reporter organoids. Impaired WNT activity, in turn, alters progenitor division angles and promotes premature neurogenesis.

Yet, this cytoskeleton–junction–WNT axis does not fully explain the extent of premature neurogenesis observed in patient-derived organoids. Multi-omics analyses uncovered a second, previously underappreciated mechanism: progressive disruption of proteostasis. We identified severity-linked upregulation of UPB and ER stress-related genes and proteins (e.g., HSPA5 (BiP), HSP90B1, DNAJB1), which intensified with severity. These alterations, indicative of chronic activation of the UPR, were not confined to early progenitors but persisted into neurons in severe LIS1 organoids, pointing to a sustained stress phenotype. Given LIS1's established role in dynein-mediated microtubule transport[5,6,8], the severity-associated reduction in LIS1 protein dosage/function, and the microtubule dependence of misfolded protein trafficking to the perinuclear region[55,56], we hypothesize that LIS1 mutations may impair aggresome formation and proteasomal clearance, thereby triggering ER stress[55,56]. While transient UPR activation is a physiological feature of early neurogenesis that promotes direct neuronal differentiation, persistent signaling can impair neurogenic timing and balance[47], potentially contributing to the premature differentiation observed in LIS1 organoids. This aligns with emerging evidence implicating sustained UPR dysregulation in neuronal pathology across various NDDs[57]. Together, these findings established proteostasis dysregulation and chronic ER stress as core, previously unrecognized mechanisms in LIS1-lissencephaly, likely acting in parallel with cytoskeletal instability to drive disease progression.

Our pharmacological rescue experiments provide functional support for this integrated model. Microtubule stabilization with EpoD restored ventricular niche integrity, while CHIR99021-mediated WNT activation selectively restored progenitor cell division mode. Most notably, mTORC1 inhibition by Everolimus significantly reduced premature neurogenesis and proteotoxic stress in moderate and severe conditions, providing evidence that targeting protein homeostasis can alleviate severity-linked alterations in LIS1-lissencephaly. Together, our integrated multi-omics and functional validation data converge on a model where the graded reduction of functional LIS1 protein levels underlies both the disruption of the cytoskeleton–junction–WNT axis and the activation of proteostasis stress responses. This integrative approach reveals that proteostasis dysregulation, as evidenced by upregulation of UPR components, is a severity-linked mechanism in LIS1-lissencephaly.

LIS1-lissencephaly shares mechanistic features with other MCD, including focal cortical dysplasia type II (FCDII), tuberous sclerosis complex (TSC), hemimegalencephaly (HME), and PIDD1-related lissencephaly. Despite divergent upstream drivers, these disorders converge on core developmental pathways, such as the WNT/β-catenin and proteostasis regulation[9,58–61]. For example, while mTOR signaling is hyperactivated in FCDII, TSC, and HME[58,59], conditions like PIDD1-related lissencephaly involve reduced pathway activity or alternate mechanisms[61]. In LIS1-lissencephaly, we did not observe primary mTOR dysregulation (data not shown), but both in silico and pharmacological analyses implicate mTORC1 as a modulator of secondary proteostasis stress. These findings suggest that disruption of proteostasis and developmental signaling contributes to a shared vulnerability across MCDs.

A key strength of this study lies in its severity-stratified design, which moves beyond conventional binary case-control models to capture the clinical heterogeneity of LIS1-lissencephaly. By systematically comparing organoids derived from multiple individuals across clinically defined mild, moderate, and severe presentations, we were able to capture non-linear relationships between genotype and phenotype, particularly where total LIS1 protein levels did not strictly correlate with clinical severity. Our data support that functional LIS1 dosage, shaped by mutation-specific effects, is a more informative determinant of disease progression than total protein abundance alone. While isogenic models remain the gold standard for isolating mutation effects, we aimed to investigate how diverse LIS1 mutations translate into a graded clinical spectrum. To ensure robustness across genetically diverse patient lines, we employed a biologically heterogeneous and age-spectrum matched[26] control pool of unrelated iPSC lines. This approach is supported by recent benchmark studies emphasizing donor diversity over clonal replication as a key factor for balancing sensitivity and specificity in phenotypic comparisons[27]. Combined with multimodal validation and pathway-specific rescue experiments, our model captures converging disease mechanisms that intensify along a severity spectrum and offers a scalable framework for dissecting genotype-informed pathophysiology in LIS1-lissencephaly and related disorders. This strategy aligns with recent non-isogenic severity-stratified organoid studies of NDDs[62,63], reinforcing the utility of this approach for dissecting relevant, mutation-specific mechanisms in genetically heterogeneous disease contexts.

In summary, our study identifies proteostasis dysregulation as a previously unrecognized, severity-linked mechanism in LIS1-lissencephaly and demonstrates that patient-derived organoids can faithfully model the clinical spectrum of this MCD. By capturing both shared and severity-linked progressive phenotypes, we show how stratified organoid modeling can uncover mechanisms underlying variable expressivity in NDDs. This approach not only advances our understanding of LIS1 pathology but also establishes a scalable framework for future mechanistic studies and the development of more personalized therapeutic strategies.

Methods

Cell lines and patients

For the human samples used in the study, all participants provided written informed consent prior to participation in the study. LIS1-

patient fibroblasts and lymphocytes were collected from Nadia Bahi-Buisson from the Necker Enfants Malades University Hospital in France (Ethics committees of the Imagine–Institut des maladies génétiques, Paris, approval no. DC2014-2272). We selected those LIS1 patients in this study for whom blood and/or fibroblast samples were available, who were clinically and genetically well-characterized, for whom high-quality MRI data were available, and for whom patient consent had been obtained. For more details see Philbert et al.[25] (LIS1-mild 1, 8-year-old male donor, c.569-10T>C *LIS1* mutation; LIS1-mild 2, 5-year-old male donor, c.569-10T>C *LIS1* mutation; LIS1-moderate 1, 6-year-old female donor, c.13delC *LIS1* mutation; LIS1-moderate 2, 13-year-old female donor, delEx11 *LIS1* mutation; LIS1-severe 1, 4-year-old female donor, c.1002+1G>T *LIS1* mutation; LIS1-severe 2, 18-year-old female donor, c.531G>C *LIS1* mutation; LIS1-severe 3, 3-yea-old female donor, c.445C>T *LIS1* mutation). Each patient-specific *LIS1* mutation was confirmed using Sanger sequencing after PCR amplification of the coding sequences. 2 control iPS cells were derived from skin fibroblasts obtained from Coriell Biorepository (control 1, 2-years old female, catalog ID GM00969, control 2, 5-month-old male, catalog ID GM08680), one control iPS cell line was received from the Cell lines and DNA bank of Rett Syndrome, X-linked mental retardation and other genetic diseases, member of the Telethon Network of Genetic Biobanks (control 8, 6-years old female, catalog no. 2271#2). An additional 5 control iPS cell lines were received from Dr. Sandra Horschitz (Ethics Committee II of Medical Faculty Mannheim of Heidelberg University, approval no. 2014-626N-MA, control 3, 21-year-old female donor; control 4, 44-year-old female donor; control 5, 25-year-old female donor; control 6, 26-year-old female donor, control 7, 23-year-old male donor).

A complete overview of the cell lines used in this study is provided in Supplementary Data S1.

Reprogramming of fibroblasts and lymphocytes

Somatic cells were reprogrammed by non-integrative delivery of OCT4, SOX2, KLF4, and c-MYC using the CTS™ CytoTune™-iPS 2.1 Sendai Reprogramming Kit (Thermo Fisher). The manufacturer's instructions were strictly followed (CTS™ CytoTune™-iPS 2.1 Sendai Reprogramming Kit User Guide).

iPSC validation and culture

Pluripotency of reprogrammed cells was quality-controlled by detection of the pluripotency-associated markers TRA-1-60, TRA-1-81, and SSEA-4 by immunocytochemistry and their capacity for spontaneous differentiation into cell types of all three germ layers. To induce 3-germ-layer differentiation, iPSCs were dissociated into single cells using TrypLE Express and plated in an ultra-low-binding 96-well plate (9000 cells/well; Amsbio, lipidure-coat plate A-U96) in Pluripro-medium (PP, Cell guidance systems) supplemented with 50 µM ROCK inhibitor to induce embryoid body (EB) formation. After 2 days, EBs were plated onto extracellular matrix (GT)-coated dishes in DMEM containing 10% fetal calf serum (FCS), 1% pyruvate, and 1% non-essential amino acids (NEAA, Gibco). Cells were cultured for 4 weeks before being subjected to immunocytochemical analysis. Further whole-genome single-nucleotide polymorphism (SNP) genotyping was performed for each iPSC line for karyotyping. To that end, genomic DNA was prepared using the Dneasy Blood & Tissue Kit (Qiagen). SNP genotyping was performed at the Institute of Human Genetics at the University of Bonn. Genomic DNA at a concentration of 50 ng/µl was used for whole-genome amplification. Afterward, the amplified DNA was fragmented and hybridized to sequence-specific oligomers bound to beads on an Illumina OmniExpressExome v1.2 chip or Illumina Infinium PsychArray-24 v1.1 chip. Data were analyzed using Illumina GenomeStudio V2011.1 (Illumina). Patient-specific LIS1 mutations were validated in the iPSC by Sanger sequencing for the *LIS1*-mutation c.13delC and c.569-10T>C, and in fibroblasts by Multiplex Ligation-dependent Probe Amplification (MLPA) for the *LIS1*-mutation: exon 11 del, c.1002+1G>T and c.445C>T. Induced PS cells were maintained on Geltrex-coated cell culture plates (Thermo Fisher) in PP medium or Essential 8 (E8) medium at 37 °C, 5% CO_2, and ambient oxygen level with daily medium change. For passaging, cells were treated with TrypLE Express (Stem Cell Technologies) or EDTA (Thermo Fisher Scientific). After passaging, the medium was supplemented with 5 µM Y-27632 (CellGuidance Systems) to foster cell survival. All human iPSC lines were regularly tested and confirmed negative for mycoplasma.

Generation of WNT-GFP reporter iPSC lines

iPSC were transduced with a Lentivirus expressing GFP under activation of WNT signaling (Lentiviral-Top-dGFP reporter, Addgene plasmid #14715). Puromycin (1 µg/ml, Sigma-Aldrich) selection was initiated 48 h following transduction. iPSC-WNT reporter lines were used for forebrain-type organoid generation.

Generation of 3D forebrain-type organoids and cortical progenitor cells

Cerebral forebrain-type organoids were generated and quality controlled as previously described[28,64]. Briefly, iPSC colonies were dissociated using TrypLE Express (Thermo Fisher Scientific), and cells were plated in U-bottom 96-well plates previously coated with 5% Pluronic F-127 (Sigma Aldrich) in phosphate-buffered saline (PBS). Cells were seeded in a volume of 150 µl/well in PP or E8 medium supplemented with 50 µM Y-27632. Following successful cell aggregation, the medium was switched at day 5 to neural induction medium (DMEM/F12, B27 supplement 1%, N2 supplement 0.5%v/v, cAMP 300 ng/ml, GlutaMAX 1%, NEEA 1%, D-Glucose, Insulin, KOSR 2%, Penicillin/Streptomycin 1% v/v, heparin 1 µg/ml, LDN-193189 0.2 mM, A83-01 0.5 mM and XAV 2 µM) with a medium change every second day. Sufficient neural induction was monitored by the development of translucent and smooth edges using a bright-field microscope. On days 9–11, when translucent neural ectoderm was visible, organoids were embedded in GT (Thermo Fisher), transferred to Pluronic F-127-coated dishes and maintained in neural differentiation medium (DMEM/F12, B27 supplement 1%, N2 supplement 0.5% v/v, cAMP 300 ng/ml, GlutaMAX 1%, NEEA 1%, D-Glucose, Insulin, KOSR 2% and Penicillin Streptomycin 1% v/v). After this passage, organoids were kept in 10 or 6 cm dishes under agitation at 70 rpm on an orbital shaker (Infors Celltron HD) at 37 °C, 5% CO_2, and ambient oxygen level. The media was changed every 3–4 days. At day 15 or 20, organoids were harvested for phenotypical analysis, while for scRNA-seq they were collected at day 20+/−3. For immunostaining, 20 µm sections were prepared using a cryotome. At least six organoids for each of three different batches were analyzed.

Induced PS cell-derived neural progenitors were generated along established protocols[30] with slide adaptations. Neural induction was initiated in 90–95% confluent iPSC cultures by changing the culture medium to neural base medium containing advanced DMEM/F12 (Thermo Fisher Scientific, 12634010) supplemented with 1% Pen/Strep, Glutamax (1x; Thermo Fisher Scientific, 35050038) and 1% B-27 supplement (Thermo Fisher Scientific; 17504044). Cells were grown in neural base medium supplemented with SB-431542 (10 µM; Cell Guidance Systems, SM33), LDN-193189 (1 µM; StemCell Technologies, 72148) and XAV939 (2 µM; Cell Guidance Systems, SM38) for 8 days. On day 8 (in case of the LIS1 moderate line 1.2, on day 6, as this line tends to prematurely differentiate), neural progenitor base medium was supplemented with LDN-193189 (200 nM) and XAV939 (2 µM). Cells were harvested for mass spectrometry 2 days after passaging and replating in neural differentiation media containing DMEM/F12, 0.5% N2 supplement, 1% B27 supplement, and cAMP (300 ng/ml) on GT-coated cell culture plates. Cells cultured in parallel were used for quality control, which included immunohistochemistry for neural progenitors and neurons. Only those batches where homogenous neural induction was confirmed were further processed for mass spectrometry. At least 4 samples derived from at least two different genetic backgrounds and generated from at least three different batches were processed for mass spectrometry.

CHIR, epothiloneD and everolimus Treatment

Organoids were treated after the induction phase, from culture day 10 to day 15 with 1 μM CHIR or 1 nM epothiloneD and fixed. For treatment with everolimus, organoids were treated from day 10 to day 19 with 20 nM everolimus, refreshing media every three days and fixed at day 20. The drugs were resuspended in DMSO to reach the concentration of 1 μM CHIR, 1 nM epothiloneD or 20 nM everolimus, respectively. After treatment, organoids were fixed and cryo-sectioned for immunocytochemical analysis.

Clearing of 3D forebrain-type organoids

For whole tissue mounting, organoids were fixed with 4% PFA for 2 h at RT and optically cleared according to Susaki et al.[65]. Blocking was done with 10% horse serum, 0.2% gelatin from cold water fish skin, and 0.1% Triton X-100 diluted in PBS for 24 h at 37 °C, followed by primary antibody incubation for 48 h at 37 °C. Secondary antibody incubation was done for 48 h at 37 °C. Refractive index matching was performed by immersion of samples in an aqueous solution of glycerol (RI = 1.457) for 48 h at RT. Samples were mounted in U-shaped 2.5 mm glass capillaries by embedding in 0.1% low-melting agarose in ddH$_2$O. For light sheet microscopy, glass capillaries were transferred into 35 mm glass bottom dishes, immobilized by agarose embedding, and immersed in RI-matched glycerol solution. For temperature adjustment, samples were kept in the microscopy room for at least 24 h before image acquisition. Image acquisition was done using a Leica Microsystems TCS SP8 DLS, equipped with LAS X software, L ×1.6/0.05 DLS illumination objective, HC APO L ×10/0.30 W DLS detection objective and 7.8 mm Glycerol DLS TwinFlect mirrors. Image stacks were acquired with a step size of 3.7 μm and fused with LAS X.

Histology and Immunocytochemistry

Cells and organoids were fixed with 4% paraformaldehyde (PFA) for 10 min at room temperature (RT) and blocked in 10% Fetal Calf Serum in PBS with 0.1% Triton for 1 h at RT. Primary antibodies were diluted according to the manufacturer's instructions and incubated overnight at 4 °C with the following dilutions: Ac-TUB (1:500, Cell Signaling, cat. no. 5335S), AFP (1:200, Sino Biologicals, cat.no. 12177-MM227, TUBB3 (1:2000, Cell Signaling, cat. no, 5666S), NANOG (1:200, DSHB, cat.no. PCRP-NANOGP1-2D8), N-CAD (1:500, BD, cat. no. 610920), p-VIM (1:500, MBL, cat. no. D076-3), TPX2 (1:500, Novus Biologicals, cat. no. NB500-179), OCT3/4 (1:500, R&D Systems, cat. no. AF1759), SMA (1:400, Abcam, cat. no. ab5694), SSEA3 (1:500, Abcam, cat. no. mc631), and SOX2 (1:500, Santa Cruz, cat. no. sc-365823), HSP90 (1:250, Genetex, cat. no. GTX109753), BiP (1:250, provided by Professor Martin Jung, University of Saarland), TBR1 (1:1000, Cell Signaling, cat. no. D6C6X), SATB2 (1:500, abcam, cat.no. ab92446), CTIP2 (1:500, abcam, cat. no. ab18465), HuC/D (1:1000, Invitrogen, cat. no. A21271), S100ß (1:500, Sigma, cat. no. S2532), SST (1:500, Millipore, cat. no. MAB354). The secondary antibodies were diluted according to the manufacturer's instructions and incubated for 1 h. at RT (488-ms/rb; 555-ms/rb/rt; 647-rb, 1:1000, Invitrogen, cat. no. A11001, A11008, A21424, A21429, A21434, A21244, respectively). Nuclei were visualized using 0.1 μg/ml DAPI (Sigma-Aldrich). Stained sections were stored at 4 °C and imaged using the Inverted Leica DMIL LED Microscope with the Thunder imaging software (Leica).

For hematoxylin–eosin staining, organoid sections were placed in ddH$_2$O for 10 s, stained with hematoxylin solution (Carl Roth) for 10 min, washed in ddH$_2$O and then rinsed under running tap water for 10 min. Slides were then twice held in 70% ethanol for 10 s and then rinsed in tap water for 10 min. Next, the slide was stained with 0.5% eosin solution (Carl Roth) for 5 min and afterwards shortly put in ddH$_2$O. For dehydration and clearing, it followed an alcohol series incubation starting with 70%, 80% and 90% ethanol solution for 10 s and then twice 100% ethanol incubation for 5 min each. Afterwards, the slides were dried and mounted with Moviol. Slides were stored at 4 °C and imaged using the inverted Leica DMIL LED Microscope with Thunder imaging software (Leica). All representative images presented in figures have been repeated at least three times in independent replicates.

Organoid quantifications

Organoid quantifications were performed as previously described[9] with slight adaptations. Images were acquired using the Inverted Leica DMIL LED Microscope with the Thunder imaging software (Leica) and analyzed using ImageJ and Imaris software. All quantifications were done in at least two genetic backgrounds per condition. For the quantification of the VZ dimension parameters, sections were stained with DAPI. Length and area measurements were performed with Image J software. For the VZ diameter, three measurements for each cortical VZ structure were performed: one straight measurement from the apical to the basal side of the VZ structure and two measurements, both starting at the apical point of the first measurement, while the basal point was located at a 45° angle on the right or left side. The mean of the three values was taken as the VZ diameter. In the case of heterogenous VZ diameter, the thickest area was considered. The VZ tissue area was defined as the ratio of the total VZ area to the ventricle area. Ac-TUB strand density was quantified by defining regions of the inner and outer 10 μm of the VZs. Intensity was measured by plot profile determination using ImageJ software and a self-designed Excel file containing formulae for background subtraction and automatic signal peak counting. The disruption diameter of N-CAD was measured at four apical membrane positions (90°, 180°, 270°, and 360°) using ImageJ software. The mean value was taken as the disruption diameter. Mitotic spindles were analyzed by immunocytochemical staining using p-VIM for marking dividing RG cells at the apical membrane and TPX2 for the visualization of the mitotic spindle.

Cortical organoid dissociation for single-cell RNA-sequencing

20+/−3-day old organoids (two or three organoids per genetic background; 2 genetic backgrounds per condition) and 60+/−3-day old organoids (three organoids per genetic background; 2 genetic backgrounds per condition) were either sliced with a scalpel and dissociated according to our already published protocol for single cell preparation[30] or processed for nuclear isolation using the 10x Genomics Chromium Nuclei Isolation Kit with RNase Inhibitor, following the manufacturer's instructions (10x Genomics, Pleasanton, CA, USA). Where applied, cells were multiplexed using the TotalSeq™ anti-human hashtag antibodies and following the manufacturer's instructions for cell hashing (Bio Legends). Single-cell or nucleus library preparation was performed using the 10x Genomics Chromium platform according to the 10x Genomics Chromium Single Cell 3' Library & Gel Bead Kit v3.1 chemistry user guide (10x Genomics). The prepared cDNA libraries were processed by the High Throughput Sequencing Unit of the Genomics & Proteomics Core Facility of the German Cancer Research Centre (DKFZ). The libraries were sequenced on two lanes of the Illumina NovaSeq 6k platform on an S1 flow cell (paired-end 28 + 94 bp).

ScRNA-seq data quality control and preprocessing

Count matrices for the single-nuclei RNA-seq day 20 dataset were generated from FASTQ files using Cell Ranger (10x Genomics), and data were analyzed with Seurat v4.0.5[66], unless stated otherwise. Features not expressed in any cell were removed, and cells were filtered individually per replicate based on the number of detected features, total UMI counts, and mitochondrial gene fraction (<10%;

detailed thresholds in Supplementary Data S22). Normalization was performed using SCTransform, regressing out cell cycle effects (S.Score–G2M.Score), and cell multiplets were excluded using DoubletFinder v2.0.3[67]. A two-step integration was performed: first within-condition, then across conditions, yielding the final Seurat object. Dimensionality reduction and neighbor graph construction were based on the first 50 principal components; clustering used a resolution of 0.15. Clusters were annotated using known marker genes, and the intermediate progenitor (IP) cluster was manually subdivided based on EOMES expression (>0.25), resulting in 10 final clusters. For the single-cell RNA-seq D65 dataset, count matrices were generated using Cell Ranger multi v8.1.0 (10x Genomics). One mild and one moderate sample were excluded due to quality control concerns. Data was analyzed with Seurat v5.0.2[66], unless stated otherwise. Cells with <1350 or >9000 detected genes or >5% mitochondrial content were removed. SCTransform normalization with regression of mitochondrial and cell cycle effects was applied. IntegrateData (30 dimensions, SCT method) was used for data integration. Neighbor search and clustering (Leiden algorithm, resolution = 0.4) were based on the first 25 principal components.

Sample preparation for mass spectrometry

Proteins from cortical progenitors were extracted from TriFast homogenized samples following the manufacturer's protocol. Dried, snap-frozen protein pellets underwent lysis through the addition of 200 µl of a 50 mM Tris–HCl buffer (pH 7.8) containing 5% SDS and cOmplete ULTRA protease inhibitor (Roche). The samples were then subjected to Bioruptor® treatment (Diagenode) for 10 min (30 s on, 30 s off, 10 cycles) at 4 °C, followed by centrifugation at 4 °C and 20,000×*g* for 15 min. Subsequently, the protein concentration in the supernatant was determined using the BCA assay according to the manufacturer's guidelines. Disulfide bonds were reduced with the addition of 10 mM TCEP at 37 °C for 30 min, and free sulfhydryl bonds were alkylated with 15 mM IAA at room temperature in the dark for 30 min. For proteolysis, 100 µg of protein from each sample was utilized following the S-trap protocol (Protifi). The protein-to-trypsin ratio was maintained at 20:1, and digestion took place for 2 h at 45 °C. The proteolysis process was terminated by acidifying the sample with formic acid (FA) to achieve a pH below 3.0. Verification of complete digestion of all proteolytic digests occurred post-desalting, utilizing monolithic column separation (PepSwift monolithic PS-DVB PL-CAP200-PM, Dionex) on an inert Ultimate 3000 HPLC (Dionex, Germering, Germany) through direct injection of 1 µg of the sample. A binary gradient (solvent A: 0.1% TFA, solvent B: 0.08% TFA, 84% ACN) ranging from 5% to 12% B in 5 min and then from 12% to 50% B in 15 min at a flow rate of 2.2 µl/min and at 60 °C was applied, with UV traces recorded at 214 nm[68].

Mass spectrometry sample analysis

A total of 1 g of the respective peptide samples underwent separation using an Ultimate 3000 rapid separation liquid chromatography (RSLC) nano system equipped with a ProFlow flow control device, in conjunction with a Q Exactive HF Orbitrap mass spectrometer (Thermo Scientific, Schwerte, Germany). Peptide concentration employed a trapping column (Acclaim C18 PepMap100, 100 µm, 2 cm, Thermo Fisher Scientific, Schwerte, Germany) with 0.1% trifluoroacetic acid (TFA) from Sigma-Aldrich, Hamburg, Germany, at a flow rate of 10 L/min. Subsequent reversed-phase chromatography (Acclaim C18 PepMap100, 75 µm, 50 cm) utilized a binary gradient (solvent A: 0.1% formic acid (Sigma-Aldrich, Hamburg, Germany); solvent B: 84% acetonitrile (Sigma-Aldrich, Hamburg, Germany) with 0.1% formic acid; 5% B for 3 min, linear increase to 25% for 102 min, a further linear increase to 33% for 10 min, and a final linear increase to 95% for 2 min followed by a linear decrease to 5% for 5 min). For MS survey scans, the parameters included operating MS in data-dependent acquisition mode (DDA) with full MS scans from 300 to 1600 *m/z* (resolution 60,000) and the polysiloxane ion at 371.10124 *m/z* as a lock mass. The maximum injection time was set to 120 ms, and the automatic gain control (AGC) was set to 1E6. Fragmentation involved selecting the 15 most intense ions (above the threshold ion count of 5E3) at a normalized collision energy (nCE) of 27% in each cycle, following each survey scan. Fragment ions were acquired (resolution 15,000) with an AGC of 5E4 and a maximum injection time of 50 ms. Dynamic exclusion was set to 15 s.

Mass spectrometry data preprocessing

All MS raw data underwent processing using Proteome Discoverer software version 2.5.0.400 (Thermo Scientific, Bremen, Germany) and were subjected to a target/decoy mode search against a human Uniprot database (www.uniprot.org, downloaded on 21 November 2019) utilizing the MASCOT and Sequest algorithm. The search parameters included precursor and fragment ion tolerances of 10 ppm and 0.5 Da for MS and MS/MS, respectively. Trypsin was designated as the enzyme with a maximum of two allowed missed cleavages. Carbamidomethylation of cysteine was set as a fixed modification, and oxidation of methionine was set as a dynamic modification. Percolator false discovery rate (strict) was established at 0.01 for both peptide and protein identification. A label-free quantification (LFQ) analysis was conducted for proteins with a minimum of two unique peptides, encompassing replicates for each condition.

Statistics and reproducibility

All statistical tests were performed two-sided with an alpha-error of 0.05 to indicate nominal statistical significance.

All quantitative data generated on organoids following immunocytochemistry were performed in batches of at least duplicates, and at least two batches per cell line were analyzed. The number of included individual data points and batches can be found in the tables summarizing each statistical analysis. Raw data were aggregated per batch, after which conditions were compared using Kruskal–Wallis- and post-hoc-pairwise Wilcoxon tests, as all observed parameters did not follow a Gaussian distribution, which was tested using the Kolmogorov–Smirnov test. Differences in proportions were tested using Chi-Square tests. All results were corrected for multiple testing using the Bonferroni correction, if not stated otherwise.

For differential expression testing in the single-cell sequencing data, an FDR-corrected *p*-value of 0.05 and an absolute log2FC larger than 0.5 were used to indicate statistical significance. Differential gene expression was tested using the FindMarkers() function in Seurat, which encompasses a Wilcoxon Rank sum test. The minimum percentage of gene expression was set to 0.25, meaning that a gene had to be expressed in at least 25% of cells in each population, therefore avoiding false positives by not testing genes with low expression.

Protein abundances were normalized and log-transformed. Wilcoxon Rank sum tests were performed to compare samples. Effect sizes were calculated by dividing the *Z* statistic by the square root of the sample size. FDR-correction was applied to correct for multiple testing, and results were filtered for an absolute effect size larger than 0.75. In addition to testing differential protein regulation, we performed a weighted correlation network analysis using WGCNA (version 1.72-1)[69]. Here, networks of co-regulated proteins are constructed based on the covariance of the normalized protein abundances. We used a soft threshold of 8, a signed TOM matrix, a minimum module size of 30 and a maximum block size of 20,000 to construct the modules. In WGCNA, modules are assigned random colors. Module eigengenes were correlated with the disease severity compared to the control condition. For significantly associated modules, in at least one of the conditions, a GO enrichment analysis was performed using the approach described below. For module hubgenes of the LIS1-associated modules, we constructed protein–protein interaction networks using the STRING database (v.11.5)[70].

Integrative Gene Ontology enrichment analysis of cellular pathways (GO) biological processes and molecular functions) of differentially regulated genes ($p_{adj} < 0.05$) and proteins ($p < 0.05$) was determined using the enrichGO() and compareCluster() functions of the R package clusterProfiler (v. 4.6.2). For this purpose, genes contributing to a GO term were retrieved using the org.Hs.eg.db package (v.3.14.0). We determined semantic overlap of enriched GO-terms using the pairwise_termsim() function of enrichplot (v.1.18.3) and visualized the results using the emapplot() function of the same package.

All representative images shown are from experiments repeated independently at least three times, with similar results.

Drug repositioning analysis

The NIH LINCS L1000 database[71] was used as a reference dataset for drug repositioning analysis in connectivity map analysis (CMap, https://clue.io, software version 1.1.1.43). The top 150 upregulated and downregulated DE genes from the RG cluster were used to generate the maximum input size for the CMap query tool. CMap allows an in-silico drug repositioning analysis by comparing expression changes of $n = 978$ landmark transcripts in response to standardized drug treatment protocols against the query differential expression signature. Resulting connectivity scores indicate rescue (negative score) or aggravation (positive score) of queried transcriptional changes by drug treatment. Next to the generation of connectivity scores for individual drugs or more general perturbagens, CMAP also provides connectivity information at the perturbagen class, mechanism of action, and pathway level, thus enabling a more general understanding of potential therapeutic targets in a phenotype. For visualization of CMap results, waterfall plots were generated using ggplot2 (v.3.4.2). Results for individual perturbagens such as pharmaceutical drugs or gene products were filtered based on negative normalized connectivity scores (NCS < 0) in all three conditions (mild, moderate, severe). Mechanism of action (MOA) results were filtered based on negative normalized connectivity scores in at least two conditions (moderate and severe).

Reporting summary

Further information on research design is available in the Nature Portfolio Reporting Summary linked to this article.

Data availability

The RNA sequencing data generated in this study have been deposited in the European Genome–Phenome Archive (EGA) database under accession code EGAS00001008227. The mass spectrometry data have been provided as Supplementary Data S23. Source data are provided with this paper.

Code availability

All original codes have been deposited at a GitHub repository and are publicly available as of the date of publication https://doi.org/10.5281/zenodo.16895539.

References

1. Lui, J. H., Hansen, D. V. & Kriegstein, A. R. Development and evolution of the human neocortex. *Cell* **146**, 18–36 (2011).
2. Severino, M. et al. Definitions and classification of malformations of cortical development: practical guidelines. *Brain* **143**, 2874–2894 (2020).
3. Francis, F. et al. Human disorders of cortical development: from past to present. *Eur. J. Neurosci.* **23**, 877–893 (2006).
4. Cardoso, C. The location and type of mutation predict malformation severity in isolated lissencephaly caused by abnormalities within the LIS1 gene. *Hum. Mol. Genet.* **9**, 3019–3028 (2000).
5. Singh, K. et al. Molecular mechanism of dynein–dynactin complex assembly by LIS1. *Science* **383**, 1431–1448 (2024).
6. Karasmanis, E. P. et al. Lis1 relieves cytoplasmic dynein-1 autoinhibition by acting as a molecular wedge. *Nat. Struct. Mol. Biol.* **30**, 1357–1364 (2023).
7. Reiner, O. & Sapir, T. LIS1 functions in normal development and disease. *Curr. Opin. Neurobiol.* **23**, 951–956 (2013).
8. Markus, S. M., Marzo, M. G. & McKenney, R. J. New insights into the mechanism of dynein motor regulation by lissencephaly-1. *eLife* **9**, e59737 (2020).
9. Iefremova, V. et al. An organoid-based model of cortical development identifies non-cell-autonomous defects in Wnt signaling contributing to Miller–Dieker syndrome. *Cell Rep.* **19**, 50–59 (2017).
10. Li, L. et al. LIS1 interacts with CLIP170 to promote tumor growth and metastasis via the Cdc42 signaling pathway in salivary gland adenoid cystic carcinoma. *Int. J. Oncol.* **61**, 129–129 (2022).
11. Liu, L. et al. The LIS1/NDE1 complex is essential for FGF signaling by regulating FGF receptor intracellular trafficking. *Cell Rep.* **22**, 3277–3291 (2018).
12. Gambello, M. J. et al. Multiple dose-dependent effects of Lis1 on cerebral cortical development. *J. Neurosci.* **23**, 1719–1729 (2003).
13. Fogli, A. et al. Intracellular levels of the LIS1 protein correlate with clinical and neuroradiological findings in patients with classical lissencephaly. *Ann. Neurol.* **45**, 154–161 (1999).
14. Corsini, N. S. & Knoblich, J. A. Human organoids: new strategies and methods for analyzing human development and disease. *Cell* **185**, 2756–2769 (2022).
15. Krefft, O., Koch, P. & Ladewig, J. Cerebral organoids to unravel the mechanisms underlying malformations of human cortical development. *Semin. Cell Dev. Biol.* **111**, 15–22 (2021).
16. Velasco, S. et al. Individual brain organoids reproducibly form cell diversity of the human cerebral cortex. *Nature* **570**, 523–527 (2019).
17. Birtele, M., Lancaster, M. & Quadrato, G. Modelling human brain development and disease with organoids. *Nat. Rev. Mol. Cell Biol.* **26**, 389–412 (2025).
18. Wimmer, R. et al. Two independent translocation modes drive neural stem cell dissemination into the human fetal cortex. Preprint at https://doi.org/10.1101/2025.01.08.631865 (2025).
19. Bershteyn, M. et al. Human iPSC-derived cerebral organoids model cellular features of lissencephaly and reveal prolonged mitosis of outer radial glia. *Cell Stem Cell* **20**, 435–449.e4 (2017).
20. Liu, J. & Silver, D. L. Founder cells shape brain evolution. *Cell* **184**, 1965–1967 (2021).
21. Fumoleau, P., Coudert, B., Isambert, N. & Ferrant, E. Novel tubulin-targeting agents: anticancer activity and pharmacologic profile of epothilones and related analogues. *Ann. Oncol.* **18**, v9–v15 (2007).
22. Pachenari, N., Kiani, S. & Javan, M. Inhibition of glycogen synthase kinase 3 increased subventricular zone stem cells proliferation. *Biomed. Pharmacother.* **93**, 1074–1082 (2017).
23. Laplante, M. & Sabatini, D. M. mTOR signaling in growth control and disease. *Cell* **149**, 274–293 (2012).
24. Barkovich, A. J., Guerrini, R., Kuzniecky, R. I., Jackson, G. D. & Dobyns, W. B. A developmental and genetic classification for malformations of cortical development: update 2012. *Brain* **135**, 1348–1369 (2012).
25. Philbert, M. et al. A novel recurrent LIS1 splice site mutation in classic lissencephaly. *Am. J. Med. Genet. A* **173**, 561–564 (2017).
26. Lo Sardo, V. et al. Influence of donor age on induced pluripotent stem cells. *Nat. Biotechnol.* **35**, 69–74 (2017).
27. Dutan Polit, L. et al. Recommendations, guidelines, and best practice for the use of human induced pluripotent stem cells for neuropharmacological studies of neuropsychiatric disorders. *Neurosci. Appl.* **2**, 101125–101125 (2023).

28. Krefft, O. et al. Generation of standardized and reproducible forebrain-type cerebral organoids from human induced pluripotent stem cells. *J. Vis. Exp.* **131**, e56768 (2018).
29. Nowakowski, T. J. et al. Spatiotemporal gene expression trajectories reveal developmental hierarchies of the human cortex. *Science* **358**, 1318–1323 (2017).
30. Jabali, A. et al. Human cerebral organoids reveal progenitor pathology in EML1-linked cortical malformation. *EMBO Rep.* **23**, e54027 (2022).
31. Eze, U. C., Bhaduri, A., Haeussler, M., Nowakowski, T. J. & Kriegstein, A. R. Single-cell atlas of early human brain development highlights heterogeneity of human neuroepithelial cells and early radial glia. *Nat. Neurosci.* **24**, 584–594 (2021).
32. Hou, P.-S., hAilín, D. Ó, Vogel, T. & Hanashima, C. Transcription and beyond: delineating FOXG1 function in cortical development and disorders. *Front. Cell. Neurosci.* **14**, 35 (2020).
33. Muralidharan, B. et al. LHX2 interacts with the NuRD complex and regulates cortical neuron subtype determinants Fezf2 and Sox11. *J. Neurosci.* **37**, 194–203 (2017).
34. Miao, N. et al. Opposite roles of Wnt7a and Sfrp1 in modulating proper development of neural progenitors in the mouse cerebral cortex. *Front. Mol. Neurosci.* **11**, 247 (2018).
35. Jain, A. et al. Morphodynamics of human early brain organoid development. *Nature* **644**, 1010–1019 (2025).
36. Poon, S., Easterbrook-Smith, S. B., Rybchyn, M. S., Carver, J. A. & Wilson, M. R. Clusterin is an ATP-independent chaperone with very broad substrate specificity that stabilizes stressed proteins in a folding-competent state. *Biochemistry* **39**, 15953–15960 (2000).
37. Bodzioch, M. et al. Evidence for potential functionality of nuclearly-encoded humanin isoforms. *Genomics* **94**, 247–256 (2009).
38. Yang, A. et al. Exploiting spatiotemporal regulation of FZD5 during neural patterning for efficient ventral midbrain specification. *Dev. Camb. Engl.* **151**, dev202545 (2024).
39. Ruan, X. et al. Progenitor cell diversity in the developing mouse neocortex. *Proc. Natl Acad. Sci. USA* **118**, e2018866118 (2021).
40. Liu, Y. et al. Translocational attenuation mediated by the PERK-SRP14 axis is a protective mechanism of unfolded protein response. *Cell Rep.* **43**, 114402–114402 (2024).
41. Boyd, J. L. et al. Human-Chimpanzee differences in a FZD8 enhancer alter cell-cycle dynamics in the developing neocortex. *Curr. Biol.* **25**, 772–779 (2015).
42. Shinde, V., Pitale, P. M., Howse, W., Gorbatyuk, O. & Gorbatyuk, M. Neuronatin is a stress-responsive protein of rod photoreceptors. *Neuroscience* **328**, 1–8 (2016).
43. Taetzsch, T., Brayman, V. L. & Valdez, G. FGF binding proteins (FGFBPs): modulators of FGF signaling in the developing, adult, and stressed nervous system. *Biochim. Biophys. Acta— Mol. Basis Dis.* **1864**, 2983–2991 (2018).
44. Cecchi, C. Emx2: a gene responsible for cortical development, regionalization and area specification. *Gene* **291**, 1–9 (2002).
45. Bennett, C. F., Latorre-Muro, P. & Puigserver, P. Mechanisms of mitochondrial respiratory adaptation. *Nat. Rev. Mol. Cell Biol.* **23**, 817–835 (2022).
46. Ladewig, J., Koch, P. & Brüstle, O. Auto-attraction of neural precursors and their neuronal progeny impairs neuronal migration. *Nat. Neurosci.* **17**, 24–26 (2014).
47. Laguesse, S. et al. A dynamic unfolded protein response contributes to the control of cortical neurogenesis. *Dev. Cell* **35**, 553–567 (2015).
48. Pawlisz, A. S. et al. Lis1–Nde1-dependent neuronal fate control determines cerebral cortical size and lamination. *Hum. Mol. Genet.* **17**, 2441–2455 (2008).
49. Marthiens, V., Kazanis, I., Moss, L., Long, K. & Ffrench-Constant, C. Adhesion molecules in the stem cell niche—more than just staying in shape?. *J. Cell Sci.* **123**, 1613–1622 (2010).
50. Stocker, A. M. & Chenn, A. Focal reduction of αE-catenin causes premature differentiation and reduction of β-catenin signaling during cortical development. *Dev. Biol.* **328**, 66–77 (2009).
51. Scuderi, S. et al. Specification of human brain regions with orthogonal gradients of WNT and SHH in organoids reveals patterning variations across cell lines. *Cell Stem Cell* **32**, 970–989.e11 (2025).
52. Kopp, M. C., Larburu, N., Durairaj, V., Adams, C. J. & Ali, M. M. U. UPR proteins IRE1 and PERK switch BiP from chaperone to ER stress sensor. *Nat. Struct. Mol. Biol.* **26**, 1053–1062 (2019).
53. Südhof, T. C. Towards an Understanding of Synapse Formation. *Neuron* **100**, 276–293 (2018).
54. Wilkens, R. et al. Diverse maturity-dependent and complementary anti-apoptotic brakes safeguard human iPSC-derived neurons from cell death. *Cell Death Dis.* **13**, 887–887 (2022).
55. Adams, C. J., Kopp, M. C., Larburu, N., Nowak, P. R. & Ali, M. M. U. Structure and molecular mechanism of ER stress signaling by the unfolded protein response signal activator IRE1. *Front. Mol. Biosci.* **6**, 11 (2019).
56. Hurwitz, B. et al. The integrated stress response remodels the microtubule-organizing center to clear unfolded proteins following proteotoxic stress. *eLife* **11**, e77780 (2022).
57. Vásquez, G. E., Medinas, D. B., Urra, H. & Hetz, C. Emerging roles of endoplasmic reticulum proteostasis in brain development. *Cells Dev.* **170**, 203781–203781 (2022).
58. Lee, W. S. et al. Cortical dysplasia and the mTOR pathway: how the study of human brain tissue has led to insights into epileptogenesis. *Int. J. Mol. Sci.* **23**, 1344 (2022).
59. Ricciardi, S. et al. Reduced AKT/mTOR signaling and protein synthesis dysregulation in a Rett syndrome animal model. *Hum. Mol. Genet.* **20**, 1182–1196 (2011).
60. Hodges, S. L. & Lugo, J. N. Wnt/β-catenin signaling as a potential target for novel epilepsy therapies. *Epilepsy Res.* **146**, 9–16 (2018).
61. Zhang, C. et al. Dysregulation of mTOR signalling is a converging mechanism in lissencephaly. *Nature* **638**, 172–181 (2025).
62. Urresti, J. et al. Cortical organoids model early brain development disrupted by 16p11.2 copy number variants in autism. *Mol. Psychiatry* **26**, 7560–7580 (2021).
63. Jourdon, A. et al. Modeling idiopathic autism in forebrain organoids reveals an imbalance of excitatory cortical neuron subtypes during early neurogenesis. *Nat. Neurosci.* **26**, 1505–1515 (2023).
64. Pollen, A. A. et al. Molecular identity of human outer radial glia during cortical development. *Cell* **163**, 55–67 (2015).
65. Susaki, E. A. et al. Whole-brain imaging with single-cell resolution using chemical cocktails and computational analysis. *Cell* **157**, 726–739 (2014).
66. Hao, Y. et al. Integrated analysis of multimodal single-cell data. *Cell* **184**, 3573–3587.e29 (2021).
67. McGinnis, C. S., Murrow, L. M. & Gartner, Z. J. DoubletFinder: doublet detection in single-cell RNA sequencing data using artificial nearest neighbors. *Cell Syst.* **8**, 329–337.e4 (2019).
68. Burkhart, J. M., Schumbrutzki, C., Wortelkamp, S., Sickmann, A. & Zahedi, R. P. Systematic and quantitative comparison of digest efficiency and specificity reveals the impact of trypsin quality on MS-based proteomics. *J. Proteom.* **75**, 1454–1462 (2012).
69. Langfelder, P. & Horvath, S. WGCNA: an R package for weighted correlation network analysis. *BMC Bioinform.* **9**, 559 (2008).
70. Szklarczyk, D. et al. The STRING database in 2021: customizable protein–protein networks, and functional characterization of user-uploaded gene/measurement sets. *Nucleic Acids Res.* **49**, D605–D612 (2021).
71. Subramanian, A. et al. A next generation connectivity map: L1000 platform and the first 1,000,000. *Profiles Cell* **171**, 1437–1452.e17 (2017).

Acknowledgements

We thank Isabell Moskal, Gina Tillmann, Helene Schamber and Elina Nürnberg for the pivotal technical support. We thank the DKFZ Single-Cell Open Lab (scOpenLab) for assistance with the scRNA sequencing experiment. We acknowledge the support of the NGS Core Facility Mannheim, Medical Faculty Mannheim of Heidelberg University. We thank Ilaria Meloni and the Cell lines and DNA bank of Rett Syndrome, X-linked mental retardation and other genetic diseases, member of the Telethon Network of Genetic Biobanks (project no. GTB24001), funded by Telethon Italy, and of the EuroBioBank network and the "Associazione Italiana Rett O.N.L.U.S."; for providing us with iPSCs. The work was supported by the Ministry of Innovation Science and Research of North Rhine-Westphalia (Junior Research Group, to J.L.), the ERA-NET NEURON, JTC 2015 Neurodevelopmental Disorders, STEM-MCD (to J.L., F.F., and N.B-B.), the EJP Rare Diseases 2020, MECPer-3D (to J.L.) and the generous financial support by the Hector Stiftung II (to J.L.). A.He. gratefully acknowledges the financial support by the "Ministerium für Kultur und Wissenschaft des Landes Nordrhein-Westfalen," the "Regierenden Bürgermeister von Berlin-Senatskanzlei Wissenschaft und Forschung," and the "Bundesministerium für Bildung und Forschung".

Author contributions

Conceptualization: L.Z., A.C.R., O.F., S.G.M., P.K., F.F. and J.L.; Methodology: L.Z., A.C.R., O.F., M.G., C.M., A.Ho., E.Z., A.J., F.M., R.W., C.B.S., A.He., A.A., S.H.W., T.R., A.R., N.B-B. and J.L.; Validation: L.Z., A.C.R., O.F., M.G.; Formal analysis: L.Z., O.F., M.G.; Investigation, L.Z., A.C.R., O.F.; ScRNA-Seq data analysis, L.Z., M.G., E.Z., A.Ho., A.C.R., J.L.; Mass spectrometry, including data analyses: C.B.S., A.He., T.R., A.R., M.G., L.Z., J.L.; Whole-exome-sequencing: C.M. and N.B-B.; Writing—original draft: O.F. and J.L.; Writing—reviewing and editing: L.Z., A.C.R., M.G., A.R., N.M., S.G.M., F.F. and J.L.; Visualization: L.Z., A.C.R., O.F. M.G. and J.L.; Supervision: J.L.; Project administration: J.L.; Funding acquisition: A.He., N.B.-B., F.F. and J.L.

Competing interests

O. F. has affiliated with Springer Nature following the completion of her work on this project. The other authors have no relevant financial or non-financial interests to disclose.

Additional information

Supplementary information The online version contains supplementary material available at https://doi.org/10.1038/s41467-025-64980-0.

Correspondence and requests for materials should be addressed to Julia Ladewig.

Peer review information *Nature Communications* thanks anonymous reviewer(s) for their contribution to the peer review of this work. [A peer review file is available].

Reprints and permissions information is available at http://www.nature.com/reprints

---

[1]Department of Translational Brain Research, Central Institute of Mental Health, Medical Faculty Mannheim, Heidelberg University, Mannheim, Germany. [2]HITBR Hector Institute for Translational Brain Research gGmbH, Mannheim, Germany. [3]German Cancer Research Center (DKFZ), Heidelberg, Germany. [4]Department of Genetic Epidemiology in Psychiatry, Central Institute of Mental Health, Medical Faculty Mannheim, Heidelberg University, Mannheim, Germany. [5]Institute of Reconstructive Neurobiology, University of Bonn School of Medicine & University Hospital Bonn, Bonn, Germany. [6]Department of Pediatric Neurology, Université Paris Descartes, Imagine Institute, Paris, France. [7]Department of Neurology, Medical Faculty and University Hospital, Heinrich Heine University Düsseldorf, Düsseldorf, Germany. [8]Department of Neurology, Ruhr University Bochum, BG University Hospital Bergmannsheil, Bochum, Germany. [9]BG University Hospital Bergmannsheil, Heimer Institute for Muscle Research, Bochum, Germany. [10]Department of Pediatric Neurology, Centre for Neuromuscular Disorders, University Medicine Essen, Duisburg-Essen University, Essen, Germany. [11]Brain and Mind Research Institute, Children's Hospital of Eastern Ontario Research Institute, Ottawa, ON, Canada. [12]INSERM UMR-S 1270 and U1341, CNRS UMR 8265, Paris, France. [13]Sorbonne University, Paris, France. [14]Institut du Fer à Moulin, Paris, France. [15]These authors contributed equally: Lea Zillich, Matteo Gasparotto, Andrea Carlo Rossetti, Olivia Fechtner. ✉e-mail: Julia.Ladewig@zi-mannheim.de